

Seminar series nr 197

Potential of Hyperion imagery for simulation of MODIS NDVI and AVHRR-consistent NDVI time series in a semi-arid region

Masoumeh Ghadiri

2010

Division of Physical Geography and Ecosystems Analysis

Department of Earth and Ecosystem Sciences

Lund University

Sölvegatan 12

S-223 62 Lund

Sweden



Potential of Hyperion imagery for simulation of MODIS NDVI and AVHRR-consistent NDVI time series in a semi-arid region

Masoumeh Ghadiri, 2010

Master degree thesis in Geomatics
Department of Earth and Ecosystem Sciences
Lund University

Supervisor
Dr. Jonas Ardö
Division of Physical Geography and Ecosystems Analysis
Department of Earth and Ecosystem Sciences
Lund University

Abstract

Long time series of satellite remotely sensed Normalized Difference Vegetation Index (NDVI) as an indicator of vegetation greenness can be used in a broad range of research topics such as climate change, vegetation dynamics and desertification monitoring.

The first phase of this study tests a practical method using Hyperion imagery onboard on Earth Observing-1 (EO1) spacecraft for simulation of MODerate resolution Imaging Spectroradiometer (MODIS) NDVI and prediction of Advanced Very High Resolution Radiometer (AVHRR) NDVI data series in a semi-arid region in New Mexico, USA in 2007. Bo-Cai (2000) introduced the main concepts of this method. He used Airborne Visible/Infra-Red Imaging Spectrometer (AVIRIS) dataset and an atmospheric radiative transfer model based on the look up table procedure for simulation of AVHRR-consistent NDVI. Here, Hyperion data and MODTRAN Organizer software (MODO) as an interface of the MODTRAN radiative transfer code for performing the atmospheric gaseous absorption corrections on the AVHRR NIR channel are instead applied. The second part, evaluates the consistency of the simulated MODIS NDVI and the predicted AVHRR NDVI time series (derived by the practical method) with time series of the real MODIS/Terra and MODIS/Aqua NDVI (16-day composites, 250 m) and the real AVHRR NDVI (biweekly, 1000 m) in two sites with different land covers (shrubland and grassland) located in the study area, in 2007. Before performing the consistency evaluation, both the simulated MODIS and predicted AVHRR NDVI data sets (with 30 m resolution) are scaled down to the resolution of the corresponding real data sets i.e., 250 m and 100 m, respectively.

The results of applying Hyperion data and MODO software in the tested method demonstrate that the MODIS NDVI and AVHRR NDVI time series can be simulated at image level (with 30 m resolution) promisingly. For example, the results of employing one of the Hyperion images over the study area (on 19 July 2007) into the method show that the bias in the prediction of AVHRR NDVI is about 27% lower compared to the case that it is estimated by MODIS NDVI. In addition, the results of the consistency evaluation based on the correlation and linear regression analysis for the time series of simulated MODIS NDVI and predicted AVHRR NDVI in a shrubland site and a grassland site in 2007, indicate that (1) the simulated MODIS NDVI values are highly correlated (0.81-0.98) with the real MODIS NDVI values, with Terra more than Aqua platforms and the root mean square error (RMSE) of the simulated values is in the range of 0.13-0.20 ndvi unit and (2) the predicted AVHRR NDVI time series is correlated with the real AVHRR NDVI, in the shrubland site higher than in the grassland site (0.87 and 0.66, respectively) while RMSE in the grassland site (0.12-ndvi unit) is lower than that in the shrubland site (0.18-ndvi unit).

However, two main limitations in the Hyperion data (disordered temporal resolution and not globally coverage) make it useless in the generating of a reliable NDVI time series by the tested method for large and long period applications. Optimistically, if some kind of hyper spectral data with high temporal resolution and global coverage in future are applied in this

method, results will have the capability of integration with real AVHRR NDVI time series for making long time series for global application.

Keywords: Hyperion, NDVI, AVHRR, MODIS, time series, MODO.

Acknowledgement

I dedicate this thesis to my lovely daughter, Sarina.

I would like to express my gratitude to a number of people whom without their support this thesis would not have been finished.

First and foremost, I am heartily thankful to my supervisor, Dr. Jonas Ardö for his guidance, support and encouragement throughout my thesis.

Many thanks go to all my teachers in my master program at Lund University, especially Dr. Lars Harrie, Dr. Lars Eklundh and Dr. Jonathan Seaquist who taught me a lot about Geomatics & Remote sensing science and techniques.

My sincere thanks go to Dr. Petter Pilesjö, national coordinator of Erasmus Mundus External Cooperation Window (EMECW, lot 8) scholarship program at Lund University and also Dr. Ulrik Mårtensson, for their supports during my master program. My studies were funded by EMECW.

I am deeply grateful to Dr. Barat Mojaradi and Dr. Bo-Cai Gao for their valuable solutions in the beginning of my thesis.

I would also like to thank Dr. Daniel Schläpfer who provided me with MODO software license and replied me kindly when I had questions.

It is my pleasure to thank Dr. Harry Lankreijer for his academic advising, Rafael Przybyszewski for his helping in my softwares requirements and Eva Kovacs for my administration needs.

Finally, I owe my deepest gratitude to my parents for their persistent supports and patience.

To the last but not the least, I thank my husband, Sadegh Jamali who has encouraged me all the times with his love, continues support and understanding. He cheered me up to finish this thesis.

Masoumeh Ghadiri

Table of Contents

CHAPTER 1: INTRODUCTION	1
1.1. INTRODUCTION	1
1.2. BACKGROUND	2
1.3. AIM.....	3
CHAPTER 2: STUDY AREA	5
2. STUDY AREA.....	5
2.1. CLIMATE.....	6
2.2. LAND COVER	7
CHAPTER 3: DATA	9
3. DATA.....	9
3.1. HYPERION ONBOARD ON EO-1 PLATFORM.....	9
3.2. AVHRR NDVI DATA ONBOARD NOAA	10
3.3. MODIS NDVI DATA	11
CHAPTER 4: METHODOLOGY	12
4. METHODOLOGY	12
4.1. AVHRR AND MODIS CHANNELS SIMULATION.....	13
4.1.1. <i>Hyperion radiance conversion</i>	13
4.1.2. <i>Channels simulation</i>	13
4.2. MODIS NDVI SIMULATION AND AVHRR NDVI PREDICTION	15
4.2.1. <i>AVHRR red channel prediction</i>	15
4.2.2. <i>AVHRR NIR channel prediction</i>	16
4.2.3 <i>AVHRR NDVI prediction</i>	17
4.3. NDVI TIME SERIES GENERATION AND CONSISTENCY EVALUATION	18
4.3.1. <i>Real NDVI time series preparation</i>	18
4.3.2. <i>Generation of simulated MODIS NDVI and predicted AVHRR NDVI time series</i>	19
4.3.3 <i>Consistency evaluation</i>	20
CHAPTER 5: RESULTS	21
5. RESULTS	21
5.1. RESULTS FOR 19 TH JULY 2007	21
5.2. RESULTS OF THE CONSISTENCY EVALUATION	31
CHAPTER 6: DISCUSSION AND CONCLUSION	39
6.1. DISCUSSION	39
6.2. SOURCE OF ERRORS AND POSSIBLE IMPROVEMENTS	41
6.3. CONCLUSION	41
6.4. RECOMMENDATIONS	41
REFERENCES	43
APPENDIX	46

Chapter 1: Introduction

1.1. Introduction

Remotely sensed vegetation indices are useful indicators of vegetation properties and greenness in the spatial and temporal domains. Among all of the indices, NDVI which is a photosynthetically based index has been applied in a broad range of studies such as global climate change, phenological and crop growth monitoring, yield prediction, drought and desertification monitoring, wildfire assessment, climatic and biogeochemical modeling (Ji et al., 2008). NDVI is also useful for estimation of fraction of Absorbed Photosynthetically Active Radiation (fAPAR), leaf area index (LAI) and Net Primary Productivity (NPP), which are utilized in evaluating the vegetation greenness (Carlson and Ripley, 1997; Tucker et al., 1985; John et al., 1995).

The AVHRR onboard National Oceanic and Atmospheric Administration (NOAA) satellite has long enough global coverage satellite based NDVI products for vegetation condition and ecosystem studies in global scales. These data series are useful for learning from past events, monitoring of current conditions (Van Leeuwen et al., 2006) and studying the trend of NDVI for detection of general changes in vegetation dynamics. But, there are some lacks in terms of quality and atmospheric corrections in AVHRR NDVI products compared with newer products from more accurate and better designed platforms such as the MODIS. The most important problem with AVHRR data is that these data are affected seriously by water vapor absorption in the atmosphere due to the wide spectral bands of AVHRR, particularly the Near Infra-Red (NIR) channel. It has been shown that NDVI measured by MODIS is higher than NDVI measured by AVHRR, because of two strong water vapor absorption region (0.82 and 0.97 μm) located in the AVHRR NIR channel, which reduce the NDVI values. In contrast, MODIS sensor has narrower channels with less water vapor absorption effect in the NIR channel, improved spatial resolution and better atmospheric corrections (Ji et al., 2008; Huete et al., 2002).

In spite of low quality and comparatively low spatial and spectral resolutions of AVHRR NDVI products, a continuation of these long-term data sets is extremely valuable for vegetation monitoring and mapping studies and other climate-related researches. Thus it seems that the integration of the AVHRR NDVI products with simulated values from newer and more accurate products like hyper spectral data can provide a suitable time series in terms of required length and quality to help us for better understanding of variations in vegetation dynamics at a finer spatial resolution. So this study tries to simulate/predict the MODIS and AVHRR NDVI time series using Hyperion imagery and examine their consistency with the real NDVI values.

In this study, first a practical method for simulation of the MODIS NDVI and prediction of the AVHRR NDVI time series (at image level) is tested by using Hyperion imagery and MODO software (see Appendix A. for a brief description) in a semi-arid region located in New Mexico, USA. Secondly, a consistency evaluation including correlation and linear regression analysis between the simulated/predicted MODIS and AVHRR NDVI time series

vs. the real values in two sites with different land covers (one shrubland and one grassland) in the study area in 2007 is performed.

1.2. Background

Satellite remote sensing as a primary used tool in different research fields can help terrestrial ecosystems scientists to better understand vegetation dynamics through time. This remotely sensed technique has different vegetation indices products with different temporal and spatial resolutions. NDVI is one of the most commonly used products.

NDVI introduced by Deering (1978) and Tucker (1979) is defined as the difference between reflectance values of NIR (0.73-1.0 μm) and Red (0.58-0.68 μm) spectral regions divided by the sum of those reflectance values as equation (1):

$$NDVI = \frac{\rho^{NIR} - \rho^{RED}}{\rho^{NIR} + \rho^{RED}} \quad (1)$$

where ρ^{NIR} and ρ^{RED} are the top of the atmosphere apparent reflectance values (unit-less ratio) of the NIR and red channels, respectively.

The AVHRR instrument onboard on NOAA satellites has provided the meteorological, cloud mapping, sea surface temperature and NDVI data since 1981. Continuation of AVHRR NDVI time series as the longest available NDVI dataset is valuable even though there are some limitations in terms of AVHRR data quality (mainly because of the water vapor absorption effects on the near infra-red channel) compared to the data of newer generation satellites. Like other techniques, there have been promising improvements in the quality of newer satellites' NDVI data in terms of spatial, temporal, radiometric resolutions compared to the older satellites' products. For example it is seen in the comparison of the quality of the MODIS and AVHRR NDVI products. But the problem with newer satellites' NDVI products is that these products are not long enough to be useable in long time period studies, effectively.

To have the benefits of long length and appropriate quality together, one solution could be the integration of older NDVI data sets such as the AVHRR NDVI with the newer data sets like the MODIS NDVI data or with the simulated AVHRR NDVI using hyper spectral data. Although integration of AVHRR and MODIS NDVI time series has several benefits there exist some difficulties in this integration. Since different sensors have different designs and different spatial, radiometric and temporal resolutions integration of these NDVI time series is not a straightforward work (Brown et al., 2008). For instance, differences in the channel positions and width for the AVHRR and MODIS sensors cause a bias between NDVI derived from MODIS versus NDVI from AVHRR (Bo-Cai, 2000). Main part of this bias comes from the impact of atmospheric gaseous absorption, mainly water vapor absorption, in the bandpasses of different sensors. The other difference between AVHRR NDVI and MODIS NDVI is the different equatorial crossing time of their platforms, which makes the combination of their NDVI time series difficult.

So far, different approaches have been used for combining the NDVI time series from different sensors. For example, Steven et al. (2003) simulated the spectral response from multiple instruments and converted NDVI data between sensors using simple linear equations. Trishchenko et al. (2002) corrected differences in the reflectance and NDVI to NOAA-9 AVHRR-equivalents by using a series of quadratic functions. Both the Steven et al. (2003) and Trishchenko et al. (2002) methods can't be used on global datasets because their approaches are dependent on the land cover and dataset (Brown et al., 2006). An experiment based on using nonlinear neural networks for identification and removing the differences in sensor design and variable atmospheric contamination from the AVHRR NDVI record was performed by Brown et al. (2008). They tried to match the range and variance of MODIS NDVI without removing the desired signal representing the underlying vegetation dynamics. This method needs appropriate inputs (data accounting for the differences between the sensors), which always are not available. There are some other efforts like Van Leeuwen et al. (2006) which tried to use simulated data for exploring the relationship between AVHRR and MODIS but these approaches are not directly useful in producing a sensor-independent vegetation dataset (Brown et al., 2008).

The actual satellite images for evaluating the agreement between the AVHRR NDVI and the MODIS NDVI based on the regression analysis have been used in Huete et al. (2002); Buheasier et al. (2003); Fensholt (2004); Gallo et al. (2004); Venturini et al. (2004); Kawamura et al. (2005); Batra et al. (2006); Be Dard et al. (2006) and Ji et al. (2008). It was shown that when the MODIS data were compared with the not corrected water vapor absorption AVHRR data, the AVHRR-NDVI values were considerably lower than the MODIS data (Huete et al., 2002; Fensholt, 2004; Ji et al., 2008) while Gallo et al. (2004) found a high similarity between the AVHRR NDVI and the MODIS NDVI in the comparisons based on the water vapor corrected AVHRR data (Ji et al., 2008).

Method used in this study can offer a way for integration of the real AVHRR NDVI time series with the predicted AVHRR NDVI data sets using simulated MODIS channels, Hyperion data and MODO software (for atmospheric gaseous corrections on the AVHRR NIR channels). So it can be said that integration of the real AVHRR NDVI with the predicted AVHRR NDVI dataset using simulated MODIS channels and Hyperion data, if successful, can have several benefits in terms of high quality, long enough length and less difficulties in the integration (such as the problems raised by the sensors' crossing times). It is noted that both the AVHRR and Hyperion sensors have the same equatorial crossing time, which is at 10:00 (see table 3.1).

1.3. Aim

The main objectives of the study are to:

- test a developed method for simulation of the MODIS NDVI and prediction of the AVHRR NDVI time series using Hyperion imaging data and MODO software in a semi-arid region.

- evaluate the consistency of the simulated MODIS NDVI and the predicted AVHRR NDVI time series with the real values in a semiarid region.

Chapter 2: Study area

2. Study area¹

A semi-arid region in New Mexico, USA is chosen as the study area mainly due to the availability of more Hyperion data in this area compared to the available data for other semi-arid regions in the world. Fig. 2.1 shows the U.S.A regions and specifically New Mexico region. Fig. 2.2 shows the New Mexico region covered by some Hyperion images.

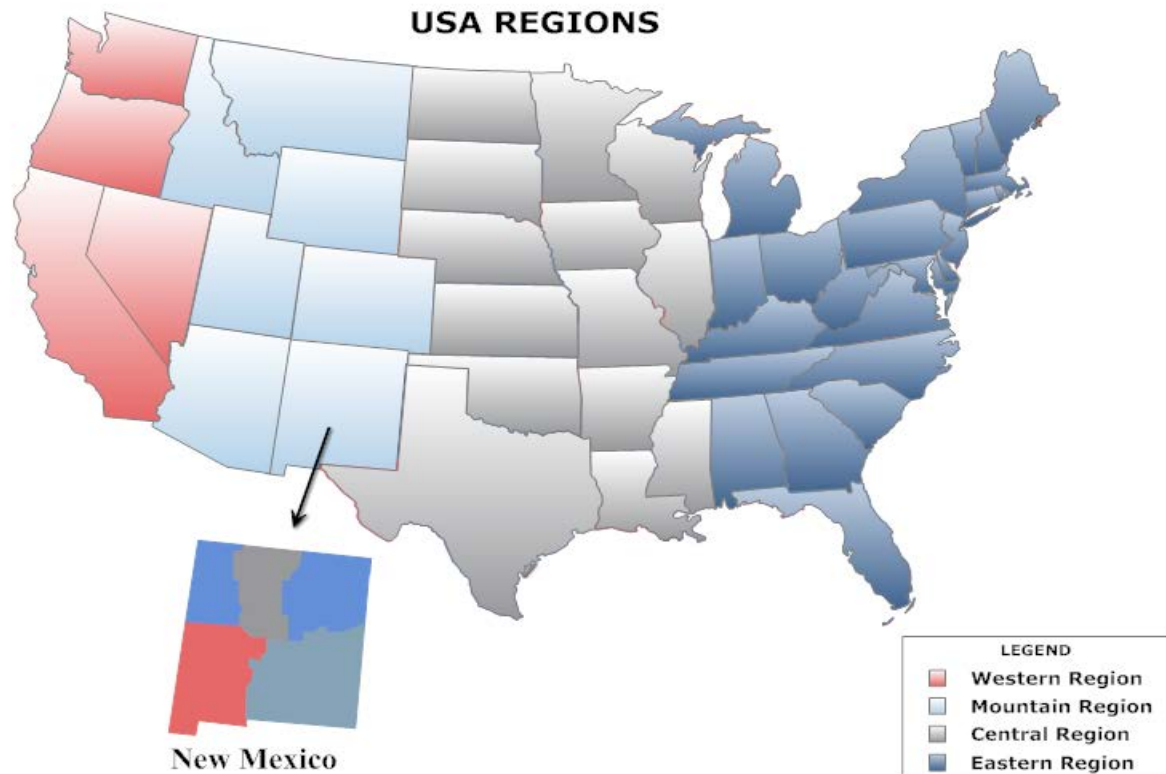


Fig. 2.1. USA regions including New Mexico².

New Mexico is located in South-Western region of the United States (fig 2.1). New Mexico has a total area of 314.460 km² and is located between latitudes 32°-37° N and longitudes 103°-109° W. High plateaus, with a lot of mountain ranges, valleys, and normally dry arroyos are the main type of State's topography. State's average elevation is about 1430 m above sea level.

¹ Source: <http://weather.nmsu.edu/News/climate-in-NM.htm>

² Made with freeware in <http://www.smartdraw.com/downloads/>

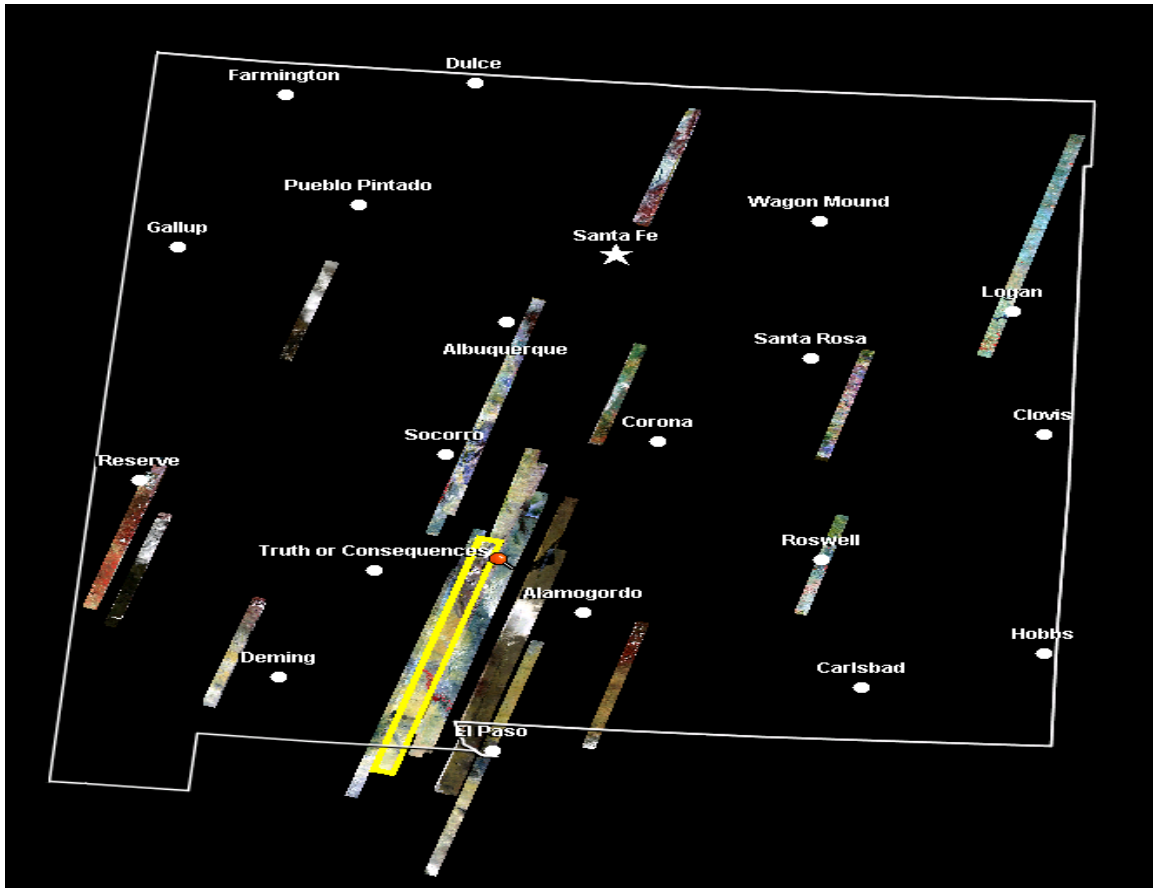


Fig. 2.2. New Mexico covered with some Hyperion images³. Highlighted area is the semi arid region chosen in study area due to maximum available Hyperion images.

2.1. Climate⁴

In general New Mexico has an arid/semiarid, continental climate. Low precipitation totals, low relative humidity, and a temperature with relatively large annual and diurnal range characterize the climate.

The average annual temperatures can range from 18°C in the southeast to less than 4°C in the northern mountains. During warmest month (July), the average monthly maximum temperature at the lower elevations in the south is about 32°C and it reaches to the upper 21°C at high elevations in the northern regions. Average temperature in daytime in January, the coldest month, ranges from 10°C to -1°C, from the southern and central valleys to the higher elevations of the north, respectively.

In New Mexico State, average precipitation is about 230 mm per year in the southern desert and central valleys. It is more than 500 mm at northern higher elevations. The rainiest months

³ Source: <http://glovis.usgs.gov/ImgViewer/Java2ImgViewer.html>

⁴ Source: <http://weather.nmsu.edu/News/climate-in-NM.htm>

in most regions of the State are July and August. These months have 30 to 40 percent of the year's total moisture falling (fig. 2.3). The driest season in New Mexico over most regions is winter. The range of average annual snowfall as the most part of winter precipitation is about 9 mm to over 250 mm, from the southern desert to northern mountain stations, respectively.

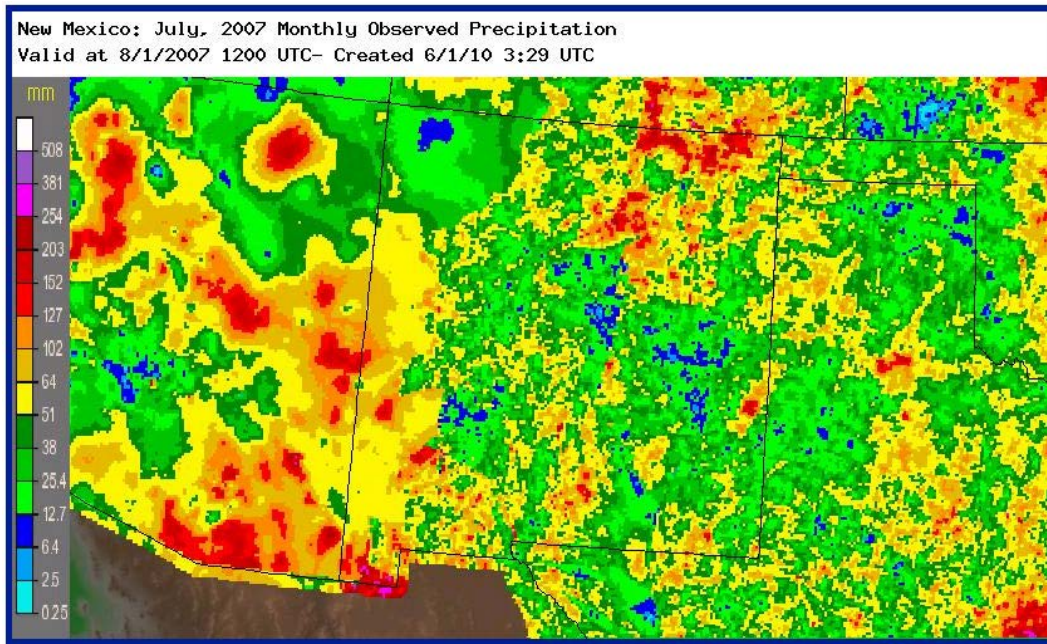


Fig. 2.3. The observed precipitation in July 2007, New Mexico ⁵.

2.2. Land cover⁶

Cultivated areas cover about 4% of the State's area. About 33% of this area is irrigated. About 50% of the State area is pastureland; about 28% is woodland and the remainder is generally classified as wasteland and urban (fig. 2.4).

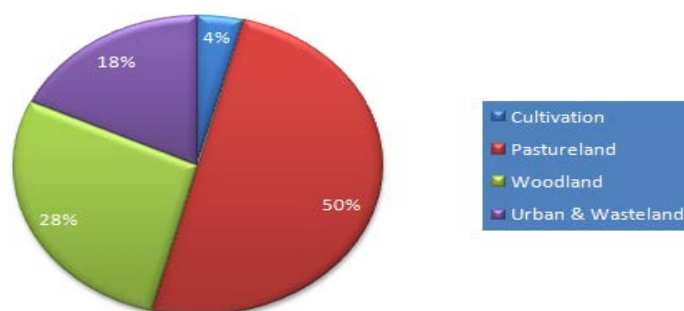


Fig. 2.4. Chart of percentage of different land cover in New Mexico.

⁵ Source: <http://water.weather.gov/precip/index.php>

⁶ Source: <http://weather.nmsu.edu/News/climate-in-NM.htm>

As can be seen in fig. 2.5, two sites with different land covers over the study area are specifically chosen for analyzing the consistency of the simulated MODIS NDVI and the predicted AVHRR NDVI time series with the real data series. The first site is located in the shrubland and the next one in grassland according to the land cover classification map of MODIS products in 2005 ⁷.

The center position coordinates of the shrubland and grassland sites are (335684E, 3562278N) and (337275E, 3567945N) in UTM 13n coordinate system, respectively.

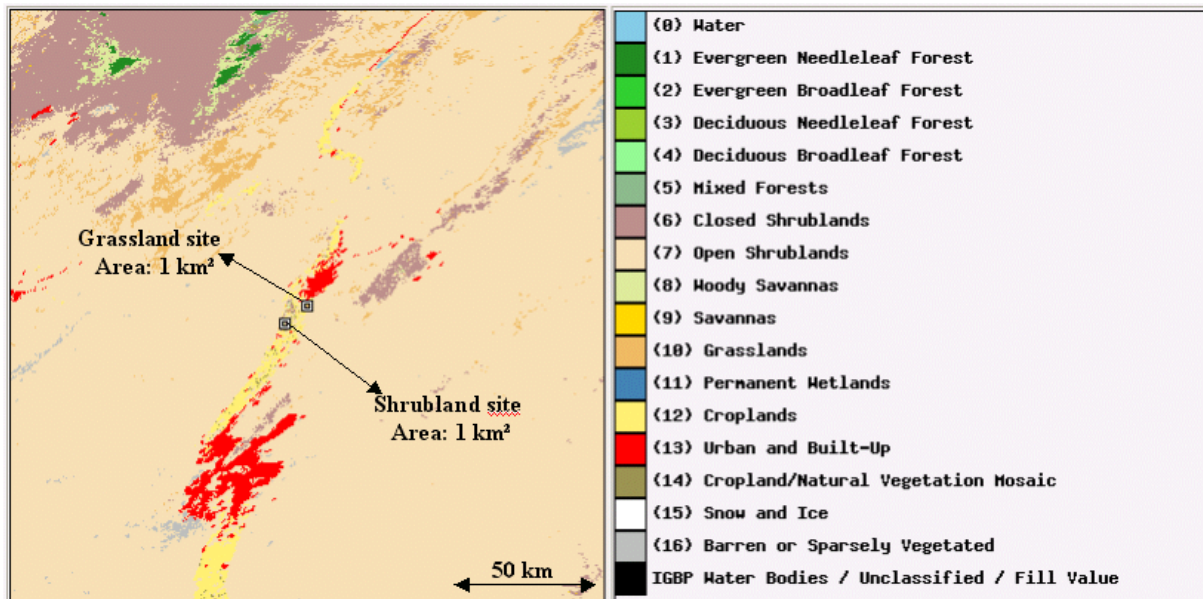


Fig. 2.5. MODIS land cover classification map of the study area including two shrubland and grassland sites ⁸.

⁷Source: <http://www-modis.bu.edu/landcover/userguidelc/>

⁸ Source:

http://daac.ornl.gov/glb_viz_2/08Sep2010_04:17:55_224896686L32.236375L-106.7271S1L1_MYD13Q1/index.html

Chapter 3: Data

3. Data

The general characteristics of the Hyperion, AVHRR and MODIS data used in this study are shown in table 3.1.

Table 3.1. General characteristics of data.

Sensor	Hyperion	AVHRR	MODIS	MODIS
Platform	EO1	NOAA-17	Terra	Aqua
Spatial resolution	30 m	1000 m	250 m	250m
Temporal resolution	At least once per month	14 day	16 day	16 day
Projection	UTM	Lambert Azimuthal Equal Area	Sinusoidal	Sinusoidal
Equatorial crossing time	~ 10:00	~10:00	~10:30	~13:30

3.1. Hyperion onboard on EO-1 platform

The Hyperion instrument onboard on EO-1 platform collects 242 unique spectral channels spanning the wavelength range from 0.357 to 2.576 μm with a 10-nm bandwidth⁹ (see Appendix B. for details). Its across-track field-of-view is 0.624-degree, which for the altitude of 705 km corresponds to a swath width of 7.6 km. The instrument can image a 7.5 km by 100 km land area per image with a 30m spatial resolution for all bands, and provide detailed spectral mapping across all 198 calibrated channels with high radiometric accuracy¹⁰.

NASA's Hyperion has two levels of products, level 1R and level 1Gst. The Level 1R radiometric product has a total of 242 bands but only 198 bands are calibrated. Level 1R is radiometrically corrected but it has no geometric corrections. Level 1Gst (with 220 bands) is terrain corrected and freely available in Geographic Tagged Image-File Format (Geo TIFF). All Hyperion data are provided in 16-bit radiance values¹¹.

Level 1Gst data is used in this study. Table 3.2 shows the standardized set of processing parameters at level 1Gst.

Hyperion data in 2007 are used in this study because there are more images over the study area in this year compared to the other years. Table 3.3 shows the list of all available Hyperion imaging data for New Mexico in 2007 used in this study.

⁹ Source, http://gcmd.nasa.gov/records/GCMD_USGS_EDC_EO1_Hyperion.html

¹⁰ Source, <http://eo1.usgs.gov/hyperion.php>

¹¹ Source, <http://edcsns17.cr.usgs.gov/eo1/products>

Table 3.2. Standardized set of Hyperion processing parameters at level 1Gst¹².

Map projection	UTM (default zone of the scene center coordinates)
Horizontal datum	WGS84
Re-sampling method	CC (cubic convolution)
Image orientation	Map (North up)
Pixel size	30 meter
Format	GeoTIFF

Table 3.3. Hyperion imaging data for New Mexico, USA (Path: 33, Row: 37)

No.	ID	Date	Clouds (%)
1	EO1H0330372007091110K6	2007.04.01	0
2	EO1H0330372007101110P1	2007.04.11	0
3	EO1H0330372007106110P1	2007.04.16	0
4	EO1H0330372007139110P1	2007.05.19	20
5	EO1H0330372007172110K7	2007.06.21	0
6	EO1H0330372007185110P1	2007.07.04	0
7	EO1H0330372007190110P1	2007.07.09	0
8	EO1H0330372007200110K7	2007.07.19	0
9	EO1H0330372007223110K7	2007.08.11	10
10	EO1H0330372007231110K6	2007.08.19	0
11	EO1H0330372007259110K6	2007.09.16	10
12	EO1H0330372007282110K6	2007.10.09	0
13	EO1H0330372007292110P1	2007.10.19	0
14	EO1H0330372007325110K7	2007.11.21	0
15	EO1H0330372007338110P1	2007.12.04	0

3.2. AVHRR NDVI data onboard NOAA

There are two widely used AVHRR long-term NDVI data sets that cover the globe from 1982: Global Inventory Modeling and Mapping Studies (GIMMS) and Land Long Term Data Record (LTDR). The GIMMS data set is the most commonly used for long-term vegetation change studies (Tucker et al., 2005) but in LTDR data set, atmospheric correction and BRDF correction are improved better than GIMMS (Pedelty et al., 2007). Since neither GIMMS NDVI nor LTDR NDVI are available for the year 2007, biweekly AVHRR NDVI composites

¹² Source, <http://edcsns17.cr.usgs.gov/eo1/products>

with 1 km resolution from United States Geological Survey's Center for Earth Resources Observation and Science (EROS) are used¹³.

EROS started to produce weekly and biweekly maximum NDVI composites AVHRR 1 km resolution data for United States and Alaska in 1989 (Eidenshink, J.C., 1992). The map projection for this data set is Lambert Azimuthal Equal Area. There are fourteen bands in this composite. The band number 6 is NDVI band and number 14 is cloud mask. To get NDVI with good accuracy, first channel 1 and 2 are calibrated and then NDVI is calculated. Finally the NDVI values are scaled to the range of 0 to 200 in this data set. This means that -1 (ndvi value) is equal to zero, 0 (ndvi value) is equal to 100 and finally 1 (ndvi value) equals to 200. The cloud mask band has values between 0 and 200. If the pixel has value less than 100, it means that this pixel is clear while the pixels with values 100 or more are clouds¹⁴.

3.3. MODIS NDVI data

MODIS NDVI onboard Terra and Aqua platforms (MOD13Q1 and MYD13Q1 products, respectively) are used here for comparing the real MODIS NDVI and simulated MODIS NDVI in two chosen sites in the study area. These products are computed from water, clouds, heavy aerosols, and cloud shadows corrected surface reflectances. Global MOD13Q1 and MYD13Q1 data are provided every 16 days (starting day 1 of the year for MOD13Q1 and 9 for MYD13Q1) at 250-meter spatial resolution as a gridded level-3 product in the Sinusoidal projection¹⁵.

¹³ Source: <http://edcsns17.cr.usgs.gov/EarthExplorer/>

¹⁴ Source: http://eros.usgs.gov/ecms/documents/products/AVHRR_Readme.doc

¹⁵ Source: https://lpdaac.usgs.gov/lpdaac/products/modis_products_table/vegetation_indices/16_day_13_global_250m/myd13q1

Chapter 4: Methodology

4. Methodology

The general work flow of the methodology is shown in fig. 4.1. This flowchart comprises of data and method sections. Hyperion, MODIS and AVHRR are the main datasets used here. The method section is divided into three main parts. In first part, AVHRR (red and NIR) and MODIS (green, red, NIR and water vapor absorption) wavelength bands are simulated using Hyperion spectrum. Then, a developed method for simulation of the MODIS and AVHRR NDVI using the simulated channels is tested in second part. In this method, prediction of the AVHRR NDVI data based on the simulated MODIS channels and MODO software is also described. The principles of this method were originally introduced by Bo-Cai (2000). He used two AVIRIS datasets and an atmospheric transfer model based on look up table procedure for atmospheric correction of gaseous absorption effects on AVHRR NIR channel but here the applicability of Hyperion data series instead of AVIRIS data sets and the capability of MODO software instead of look up table procedure for reducing the atmospheric gaseous absorption effects is examined. Finally, the simulated MODIS NDVI and the predicted AVHRR NDVI time series are scaled down to the resolution of the corresponding real datasets in order of consistency evaluation analysis between the real data and the simulated/predicted data series.

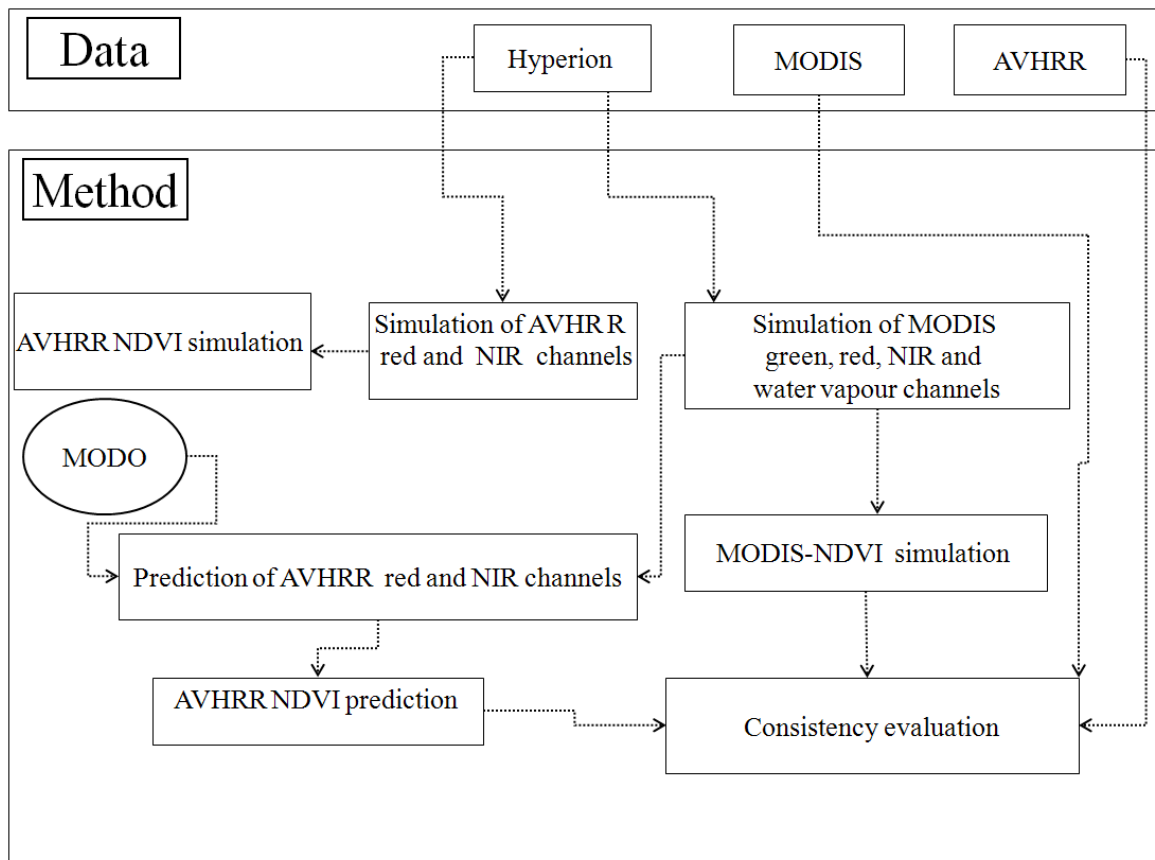


Fig. 4.1. The general flow work of the methodology.

4.1. AVHRR and MODIS channels simulation

4.1.1. Hyperion radiance conversion

Regarding equation (1), all the required Hyperion channels for simulation of the AVHRR (red and NIR) and MODIS (green, red, NIR and water vapor absorption) channels are converted from radiance values to the top of atmosphere reflectance. To have the Hyperion channels in reflectance values, first the digital values of SWIR and VNIR bands are converted to radiance values according to their scaling factors which are 80 and 40, respectively. Then radiance values are converted to the top of atmospheric reflectance values using equation (2)¹⁶.

$$\rho = \frac{(\pi \times L_{\lambda} \times d^2)}{(ESUN_{\lambda} \times \cos(\theta_s))} \quad (2)$$

where ρ is the unitless planetary (top of atmosphere) reflectance, L_{λ} is spectral radiance ($W \cdot sr^{-1} \cdot m^{-2}$) at sensor's aperture, d is Earth-Sun distance in astronomical unit, θ_s is solar zenith angle in degrees and $ESUN_{\lambda}$ ($W \cdot \mu m^{-1} \cdot m^{-2}$) is mean solar exoatmospheric irradiances.

Earth-Sun distance and solar zenith angle are the same for all channels in one Hyperion image but spectral radiance and mean solar exoatmospheric irradiances are channel depended. Earth-Sun distance for each day of the year is derived from the nautical handbook or interpolated from values listed in Appendix C. Solar zenith angle is found in the metadata file downloaded simultaneously by the Hyperion channels. Mean solar exoatmospheric irradiances for every channel are put in Appendix D. A metadata file of Hyperion data as instance is included in Appendix E.

4.1.2. Channels simulation

AVHRR red and NIR channels and MODIS red, green, NIR and water vapor absorption channels (see table 4.1.) are directly simulated through simple integration and averaging of several narrower calibrated Hyperion channels within the corresponding AVHRR and MODIS spectral bandpasses (see fig. 4.1).

Table 4.1. Characteristics of relevant AVHRR and MODIS channels.

Sensor	Green (μm)	Red (μm)	NIR (μm)	Water Vapor (μm)
AVHRR	-----	0.58-0.68	0.73-1.0	-----
MODIS	0.545-0.565	0.62-0.67	0.841-0.872	0.915-0.965

¹⁶ Source: <http://edcsns17.cr.usgs.gov/eo1/faq.php?id=21>

Details of the Hyperion channels used for directly simulation of each AVHRR and MODIS channel are shown in the table 4.2. This table also includes the number of calibrated and not-calibrated Hyperion channels within each wavelength bands. In this study, not-calibrated channels are not used in the AVHRR and MODIS channels simulation.

Table 4.2. Details of Hyperion channels used for simulating AVHRR and MODIS channels.

Sensor	Channel	Hyperion Wavelength (µm)	Hyperion Bands	Number of Bands	Number of Calibrated Bands	Not Calibrated Bands
AVHRR	Red	0.579-0.681	23-33	11	11	-----
	NIR	0.732-1.006	38-65 & 71-86	44	30	58-65 & 71-76
MODIS	Green	0.548-0.569	20-22	3	3	-----
	Red	0.620-0.671	27-32	6	6	-----
	NIR	0.844-0.872	49-51 & 71-73	6	3	71-73
	Water Vapor	0.915-0.962	56-61 & 78-82	11	7	58-61

Fig. 4.2 shows the position of the relevant AVHRR and MODIS bandpasses as well as the mean apparent reflectance values of the Hyperion spectra in the wavelength region of 500-1000 nm over an image of the study area in July 19, 2007.

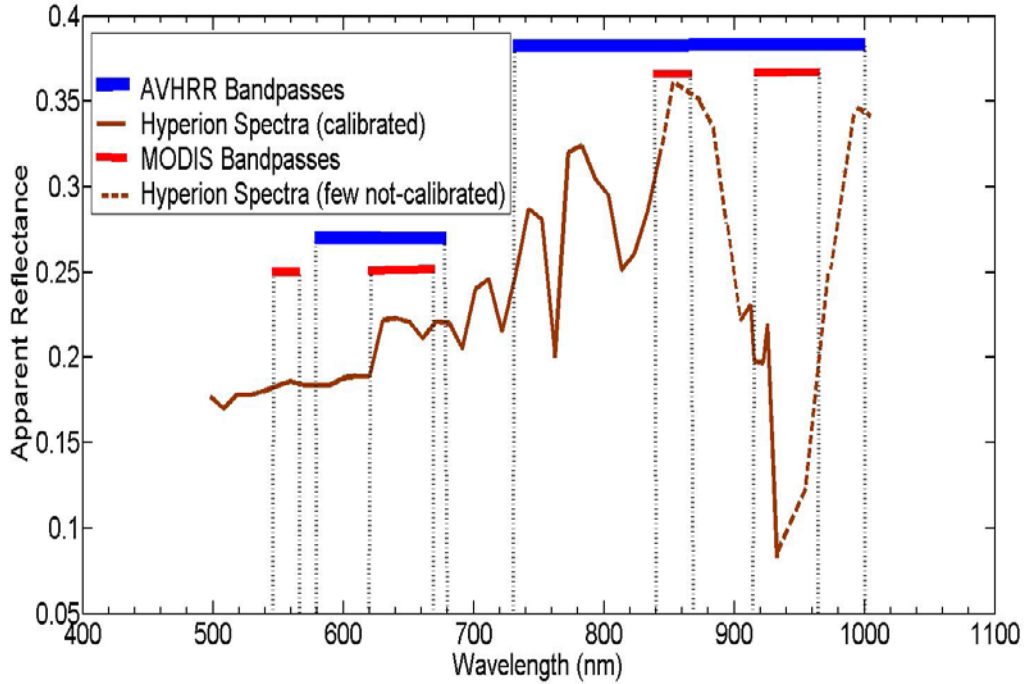


Fig. 4.2. Example of apparent reflectance spectra acquired with the Hyperion instrument over the study area in July 19, 2007 (c.f.(Bo-Cai, 2000)). AVHRR and MODIS bandpasses (blue and red lines) just represents AVHRR and MODIS channel regions, respectively and they don't have specific reflectance levels on vertical axis.

As can be seen, by the strong reflectance dip of the Hyperion spectra around 950 nm, in fig. 4.2, water vapor absorption has significant effects in the AVHRR NIR channel rather than MODIS NIR channel. Thus for the AVHRR NDVI prediction using Hyperion data, the impacts of water vapor absorption (mainly in the AVHRR NIR) should be properly taken into account.

4.2. MODIS NDVI simulation and AVHRR NDVI prediction

MODIS NDVI is easily simulated using already simulated red and NIR channels by substituting in the equation (1). But for prediction of the AVHRR NDVI, following steps are performed.

4.2.1. AVHRR red channel prediction

Now, simulated MODIS red and green channels are used in a linear combination equation for prediction of the AVHRR red channel based on the weighted averaging method (Bo-Cai, 2000). This linear equation is:

$$AVHRR_{red} = a \times MODIS_{green} + b \times MODIS_{red} \quad (3)$$

where the weighting coefficients a and b are 0.17 and 0.83, respectively. Regarding these coefficients, the impact of MODIS red channel on the averaged value (AVHRR red) is larger than the impact of MODIS green channel and this is reasonable because the MODIS red

channel is wider than the MODIS green channel. It means that the weight of MODIS red information on the simulated AVHRR red channel is more than the relatively less information in the thinner MODIS green channel. By considering the center positions of AVHRR red, MODIS green and red channels on wavelength axis (see fig. 4.2) the coefficients a and b by using a simple distance ratio can be derived. This means that the weighting coefficient a is derived by dividing the distance between the center positions of MODIS and AVHRR red channels to the distance between the center positions of MODIS red and green channels. The weighting factor b is similarly considered as the ratio of the distance between the center positions of MODIS green and AVHRR red channels over the distance between the center positions of MODIS red and green channels.

4.2.2. AVHRR NIR channel prediction

In this step, simulated MODIS NIR and water vapor absorption channels calculated from averaging the Hyperion channels are used in the prediction of AVHRR NIR channel. In this prediction the effects of atmospheric gaseous absorption particularly Oxygen and water vapor must be properly taken into consideration.

4.2.2.1. Atmospheric gaseous transmittance

An atmospheric gaseous transmittance model in MODO software version 3.0 is used to correct the water vapor and Oxygen absorption effects in the bandpass of the AVHRR NIR channel (c.f. Appendix A for workflow in MODO).

To do this, water vapor amount in the Sun-surface-sensor path for each pixel is needed among other required geometry parameters. The required Sun-Surface-Sensor geometry parameters are available in the metadata files (c.f. Appendix E). This is good to mention here that since the unit of the parameters in the metadata file is different from the unit of input parameters in MODO, so unit conversion must be done, first.

The ratio of the MODIS water vapor channel over the MODIS NIR channel in reflectance unit is in relation with the water vapor amount in the Sun-surface-sensor path. This relation can be expressed by an exponential formula: (Kaufman and Gao, 1992)

$$T_w = \exp(\alpha - \beta\sqrt{W}) \quad (4)$$

where T_w (unitless) is the proportion of MODIS water vapor to the MODIS NIR channels, W is the amount of water vapor in g.cm^{-2} , $\alpha=0.02$ and $\beta=0.651$. By having the T_w and α and β , the water vapour amount (W) in each pixel is easily derived via equation (4).

Fig. 4.3 shows the dependence of reflectance ratio (T_w) on the amount of water vapors in the vertical column according to the equation (4).

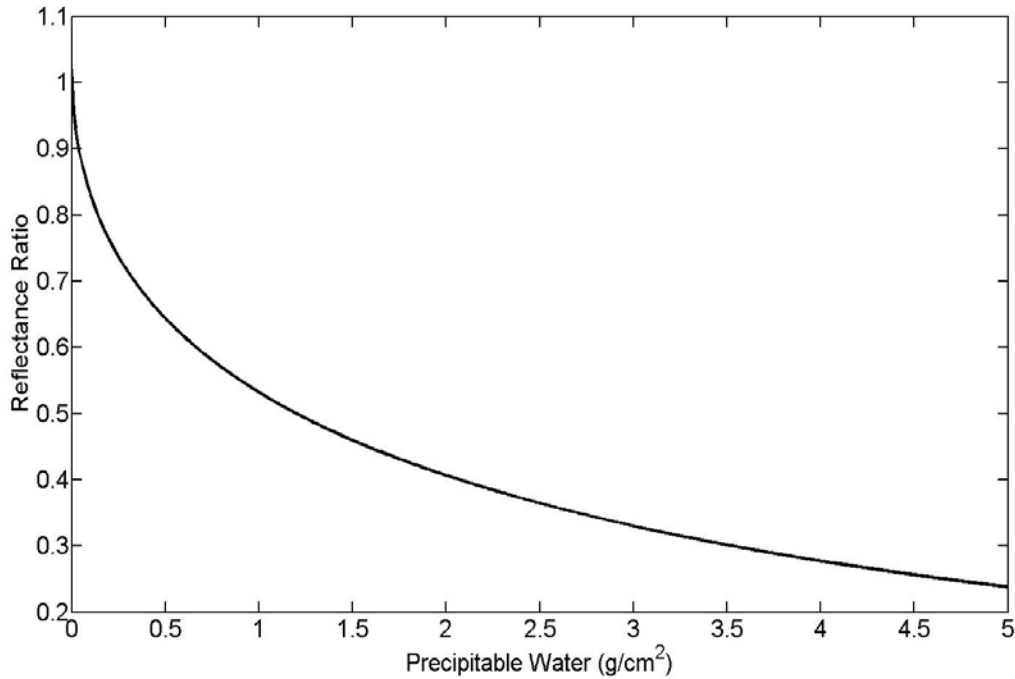


Fig. 4.3. Relation between reflectance ratio (T_w) and vertical column water vapor amount, Y-axis and X-axis, respectively.

According to the fig. 4.3 the reflectance ratio (T_w) and the amount of water vapor are inversely related, i.e., the higher reflectance ratio the lower water vapor in the Sun-surface-sensor path and vice versa.

Now, with derived water vapor amount from equation (4) and the Sun-Surface-Sensor geometry parameters from metadata file, the water vapor and Oxygen transmittances as the most important gaseous transmittance spectrums in the 730–1000 nm spectral region are estimated using MODO (c.f. Appendix A for workflow).

Then the atmosphere gaseous transmittance spectrum, which is the multiplication (mathematical product) of estimated water vapor spectrum by the Oxygen transmittance spectrum, is obtained. The obtained spectrum varies with wavelength so it is a function of wavelength.

4.2.2.2. Channels prediction

It is assumed here that the apparent reflectance of AVHRR NIR channel in the 0.73–1.0 μm region as a function of wavelength is equal to the apparent reflectance of the MODIS NIR channel (0.841–0.876 μm) in the absence of any atmospheric gaseous absorption. To have the simulated AVHRR NIR spectrum (0.73–1.0 μm region) in the presence of atmospheric gaseous absorption, the assumed apparent reflectance (without gaseous absorption) is multiplied with the recently derived gaseous transmittance spectra (Bo-Cai, 2000).

4.2.3 AVHRR NDVI prediction

By averaging the predicted apparent reflectance spectrum of AVHRR in the 0.73–1.0 μm region, the mean apparent reflectance of the broad AVHRR NIR channel (at pixel level) is

obtained (Bo-Cai, 2000). Now, the predicted AVHRR NDVI value for the considered pixel can be easily calculated using equation (1) when we have already predicted the AVHRR red and NIR channels in the reflectance values.

Ultimately, for obtaining the AVHRR NDVI for all pixels within one Hyperion image (at image level), it is required to compute the mean apparent reflectance of the broad AVHRR NIR channel for all pixels and this needs to generate the atmospheric gaseous transmittance spectrums for all pixels. Since the MODO software so far does not have the capability of image-based computations (it has been confirmed with the code author), in this study I use the mean value of the proportions of MODIS water vapor reflectance over the MODIS NIR reflectance in all pixels (i.e., averaged T_w) in equation (4) in order of obtaining the mean value of water vapor amount in all pixels within every Hyperion image of the study area. Then the above-mentioned procedure for obtaining the image of mean apparent reflectance of the AVHRR NIR channel is repeated by using this mean water vapor value in MODO and generating one averaged atmospheric gaseous transmittance spectra for all pixels. It is mentioned that Sun-Surface-Sensor geometry parameters used in MODO are the same for all pixels within one Hyperion image.

4.3. NDVI time series generation and consistency evaluation

In this step, first time series of real MODIS NDVI (Terra and Aqua) and real AVHRR NDVI in the chosen shrubland and grassland sites in 2007 are prepared. Then, for comparison purposes, time series of already simulated MODIS NDVI (30 m resolution) and predicted AVHRR NDVI (30 m resolution) at two sites are generated. Since the spatial resolutions of the real and the simulated/predicted NDVI values are not the same, simulated NDVI images are scaled down into the corresponding real images resolutions (i.e. 250 m for MODIS NDVI and 1000 m for AVHRR NDVI).

4.3.1. Real NDVI time series preparation

4.3.1.1. MODIS NDVI time series

16-day composites MODIS NDVI (Terra and Aqua) data series with 250 m resolution (MOD13Q1 and MYD13Q1 products, respectively) for the chosen sites in 2007 are downloaded (see chapter 3.3).

4.3.1.2. AVHRR NDVI time series

Biweekly AVHRR NDVI composites with 1 km resolution from EROS are used here. These real data are in the Lambertian Azimuthal Equal Area projection. For being able to compare these data with the predicted AVHRR NDVI data, they must be at the same coordinate system. Here, real AVHRR NDVI data are re-projected to UTM then time series of NDVI values at the shrubland and grassland sites are easily extracted via their coordinates.

4.3.2. Generation of simulated MODIS NDVI and predicted AVHRR NDVI time series

In this study, time series of the simulated MODIS NDVI and the predicted AVHRR NDVI at the sites in 2007 are generated. Since the real MODIS and AVHRR NDVI time series are in 250m and 1000m resolutions, respectively, the simulated MODIS NDVI and the predicted AVHRR NDVI data (both with 30m resolution) must be down-scaled to the corresponding real data resolutions. Fig. 4.4 shows the down-scaling procedure of the predicted AVHRR NDVI image over the study area in 19th July 2007, schematically.

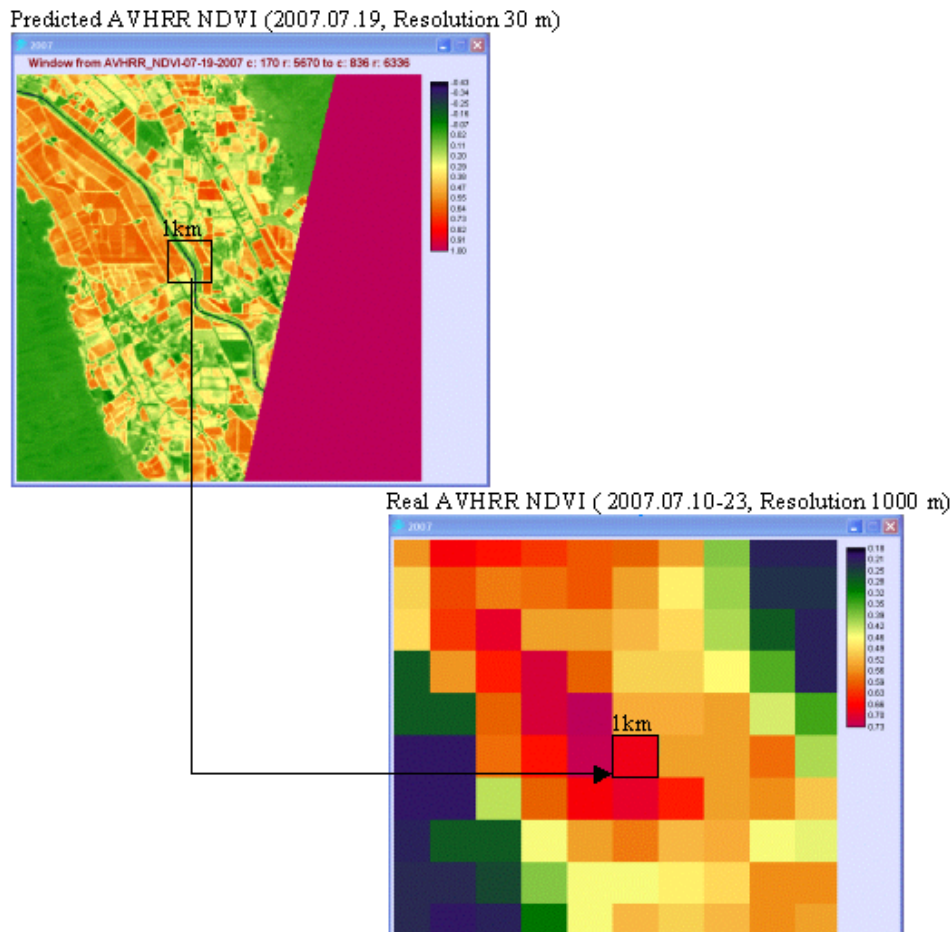


Fig 4.4. Predicted AVHRR NDVI (top) v.s Real AVHRR NDVI (bottom).

For down-scaling the simulated MODIS NDVI image from 30 m to 250 m resolution, first the image is resized to a smaller size for fast processing. Then the shrubland site and the grassland site are digitized to an area of 8 by 8 pixels. Then, the polygons vector sites are rasterized to raster files.

Now, time series of the simulated MODIS NDVI in the sites can be made in 'profile generator' of 'GIS Analysis menu' in IDRISI. To do this, first the time series file must be created. It can be done in IDRISI Explorer. The time series file is a text file with ". ts" extension that includes the number of images in the series and the name of images in each line. In 'profile generator' menu, time series option for profile type and 'mean' option for

summary type are selected. By choosing the 'mean' option the average value of those 8 by 8 pixels is computed as the new pixel value in the down-scaled image.

The same procedure is done for down scaling of the predicted AVHRR NDVI image from the resolution of 30 m to 1000 m. In this case 33 by 33 pixels are digitized instead.

4.3.3 Consistency evaluation

In this part, a consistency analysis between the simulated MODIS NDVI (down-scaled to 250 m) and the real MODIS (Aqua & Terra) NDVI (250 m) times series and also between the predicted AVHRR NDVI (down-scaled to 1000 m) and the real AVHRR NDVI (1000 m) is performed in the shrubland and the grassland sites in 2007.

In this analysis, Pearson correlation coefficients (defined by the equation 5) between the simulated/predicted NDVI values and the corresponding real values are computed. In addition, the root mean square error (RMSE) as a measure of the difference between simulated/predicted values and real values is computed. Obviously, the lower RMSE means the better estimation of the real NDVI values. RMSE is defined with equation (6).

$$Corr(X, Y) = \frac{Cov(X, Y)}{\sigma_X \times \sigma_Y} \quad (5)$$

where X denotes time series of the simulated/predicted NDVI values and Y denotes the real NDVI time series. σ_X and σ_Y are standard deviation of X and Y vectors.

$$RMSE = \sqrt{\frac{\sum_{i=1}^n (X_i - Y_i)^2}{N}} \quad (6)$$

where N is the length of each time series.

A linear regression analysis indicating the linear relationship between the simulated/predicted and real values for both the MODIS and AVHRR NDVI time series in two sites in 2007 is performed as well.

Chapter 5: Results

5. Results

The method described so far for simulation of the MODIS NDVI and prediction of the AVHRR NDVI has been applied to all Hyperion data over the study area in 2007 (see table 3.3). As instance, the results obtained for one of these images on 19 July 2007 are represented in the following, first. Then, the results of the consistency evaluation analysis between the real and the simulated/predicted MODIS and AVHRR NDVI time series (obtained from applying all the Hyperion images in 2007) for the shrubland and grassland sites are shown.

5.1. Results for 19th July 2007

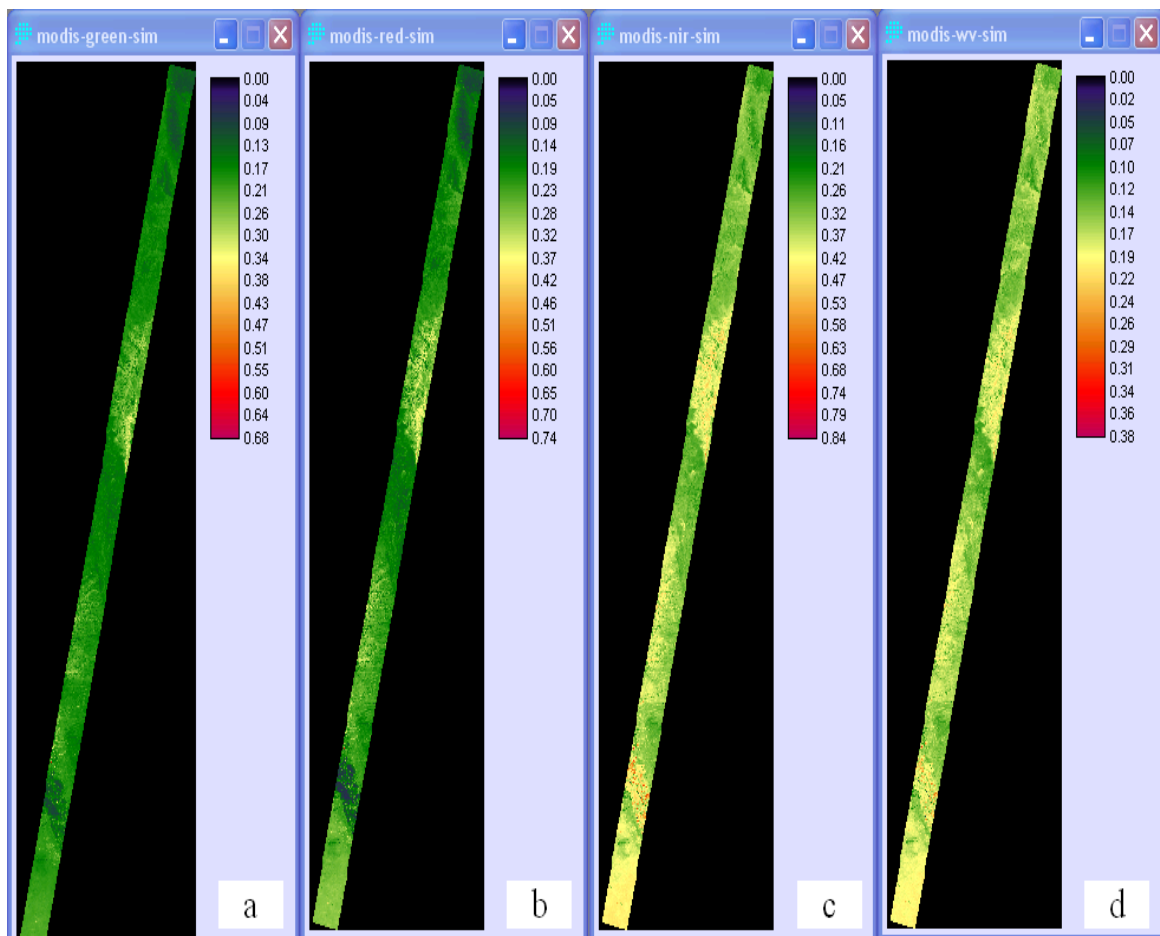


Fig. 5.1. Simulated MODIS reflectances calculated directly from the Hyperion spectra, (a) MODIS green, (b) MODIS red, (c) MODIS NIR and (d) MODIS water vapor channels, New Mexico, 19-07-2007.

Fig. 5.1 shows simulated MODIS green, red, NIR and water vapor absorption channels (in reflectance values) calculated directly through simple integrating and averaging of the Hyperion spectra over the corresponding bandpasses.

The simulated AVHRR red and NIR reflectances calculated directly from Hyperion channels are represented in fig. 5.2 (a & b), respectively. Vertical column water vapor amount (g.cm^{-2}) (for the entire column from ground to satellite) in the entire Hyperion image of the study area on 19 July 2007 is shown in fig. 5.2 (c).

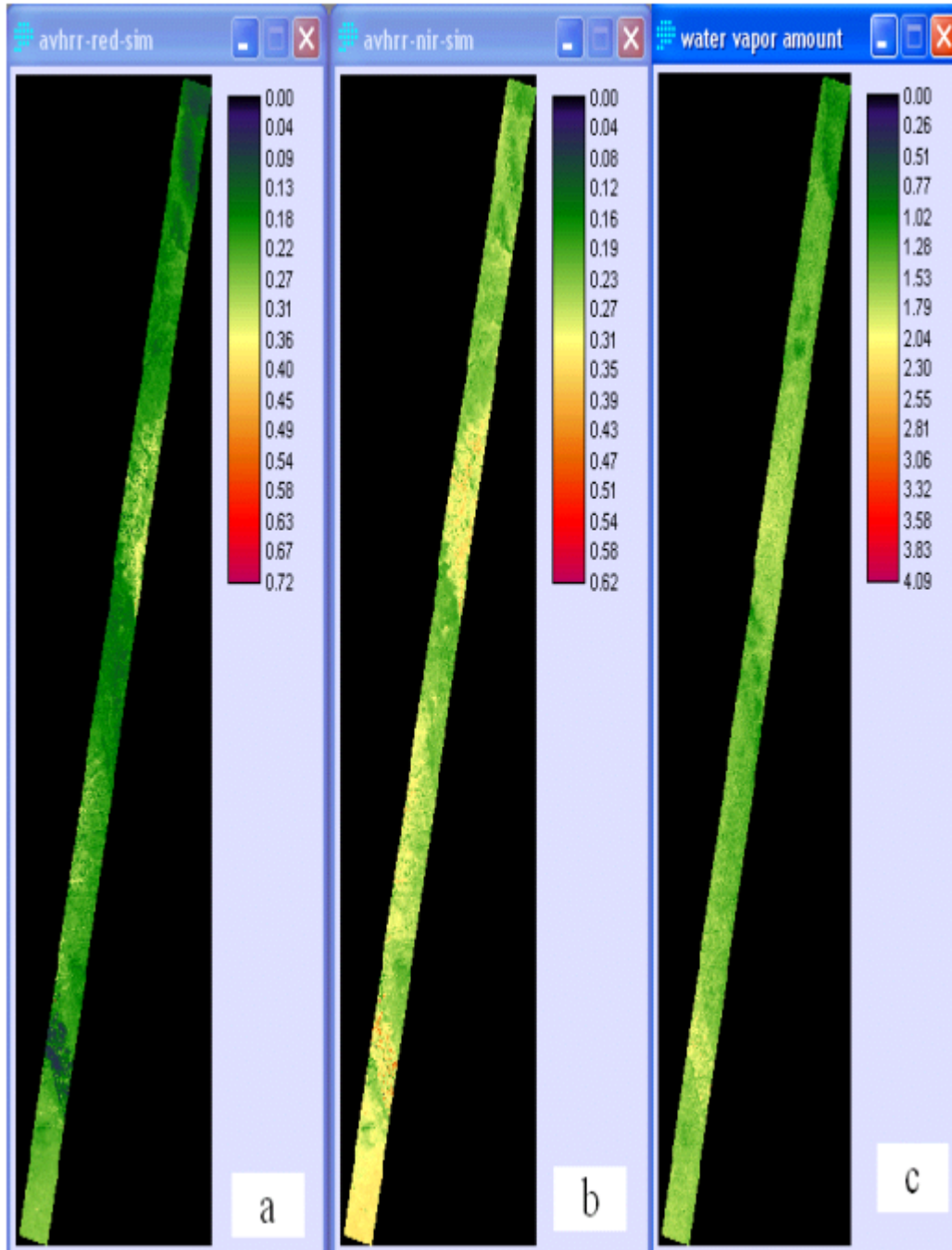


Fig. 5.2. (a) Simulated AVHRR red, (b) simulated AVHRR NIR channels calculated directly from Hyperion channels and (c) vertical column water vapor amount (g.cm^{-2}), New Mexico, 19-07-2007.

In the rest of study, these simulated mean apparent reflectance values are used in the simulation of the MODIS NDVI and prediction of the AVHRR NDVI. Table 5.1 shows the proportion of the reflectance values in the MODIS water vapor channel to the reflectance

value in the MODIS NIR channel (T_w), vertical column water vapor amount and averaged atmospheric transmittance spectrum in the 0.73-1.0 μm region for the selected Hyperion image over the study area, in 19-07-2007. It is seen that T_w ratio and water vapor amount are negatively related while T_w and atmospheric transmittance spectrum (mean value in 0.73-1.0 μm , c.f. fig. 5.4) are positively related.

Table 5.1. Proportions of reflectance in the MODIS water vapor channel to the reflectance in the MODIS NIR channel (T_w), water vapor amount and averaged atmospheric transmittance spectrum in the 0.73-1.0 μm region, New Mexico, 19-07-2007.

T_w Ratio	Water Vapor amount ($\text{g}\cdot\text{cm}^{-2}$)	Averaged Atmospheric Transmittance Spectrum in the 0.73–1.0 μm region (unitless)
Min: 0.274	4.086	0.636
Mean: 0.463	1.49	0.671
Max: 0.999	0.001	0.847

Fig.5.3 shows water vapor absorption and Oxygen transmittance spectrums derived by MODO software for the mean value of water vapor amount ($1.49 \text{ g}\cdot\text{cm}^{-2}$) in the entire scene, 19-07-2007.

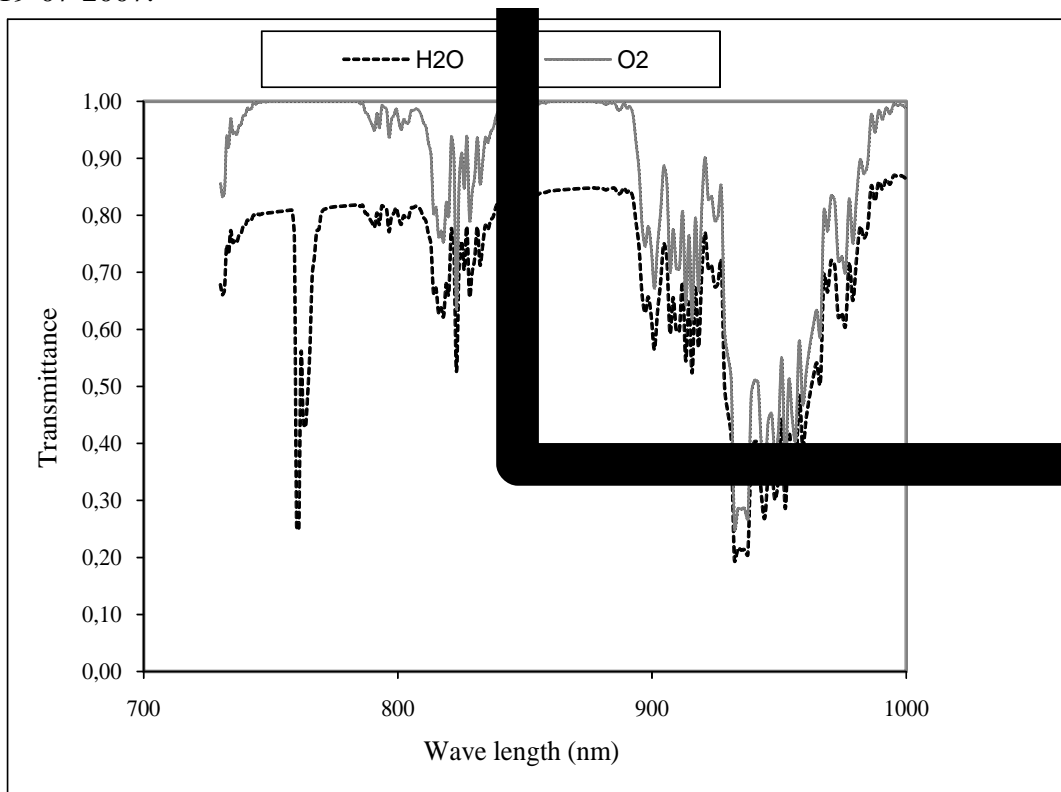


Fig. 5.3. Water vapor absorption and Oxygen transmittance spectrums derived by MODO, New Mexico, 19-07-2007.

Water vapor absorption, Oxygen and their composite transmittance spectra (the product or multiplication of water vapor and Oxygen) as atmospheric gaseous transmittance spectrum (unitless) derived from MODO for the mean value of water vapor amount (1.49 g.cm^{-2}) in entire the scene are shown in fig. 5.4.

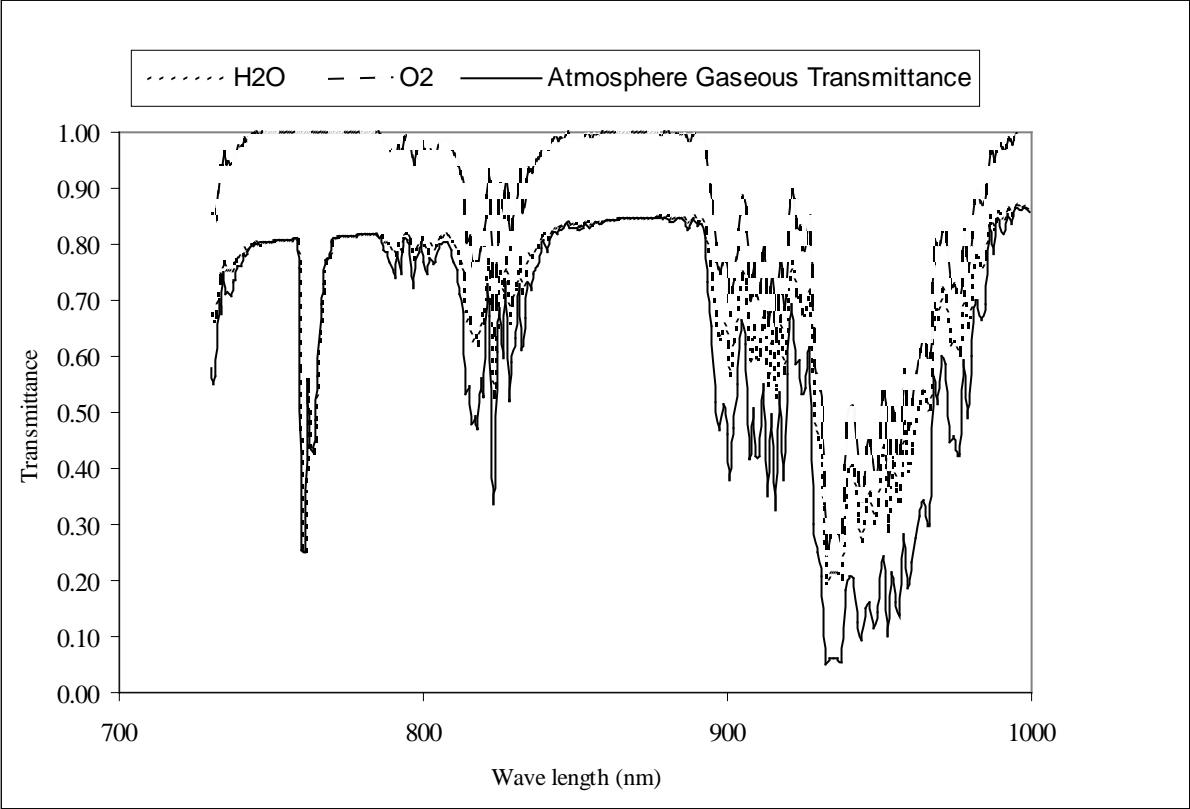


Fig. 5.4. Water vapor absorption, Oxygen and atmospheric gaseous spectrums derived by MODO, New Mexico, 19-07-2007. Atmospheric gaseous spectrum is the product (multiplication) of Oxygen and water vapor absorption spectrums.

The predicted AVHRR red channel through weighted averaging of simulated MODIS green and red channels is shown in fig. 5.5 (a). Fig. 5.5 (b) shows the AVHRR NIR channels predicted with simulated MODIS NIR and water vapor channels.

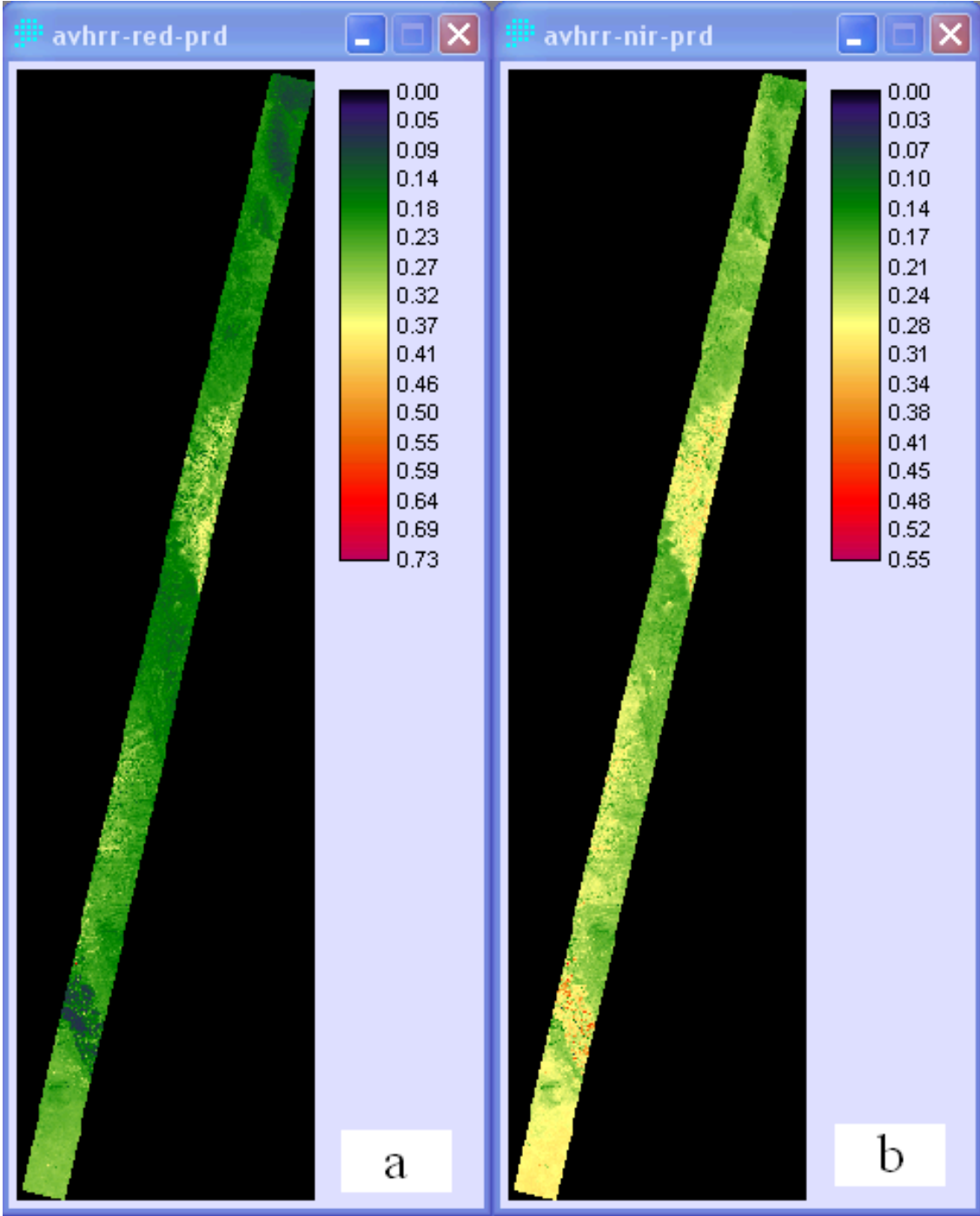


Fig. 5.5. (a) Predicted AVHRR red from the simulated MODIS green and red channels and (b) Predicted AVHRR NIR channel from the simulated MODIS NIR and water vapor absorption channels, New Mexico, 19-07-2007.

Finally, directly simulated MODIS and AVHRR channels (from Hyperion spectra) are used in the simulation of MODIS and AVHRR NDVI (fig. 5.6a and 5.6. b). Predicted AVHRR NDVI is obtained from the MODIS green, red, NIR and water vapor absorption channels (fig. 5.6 c).

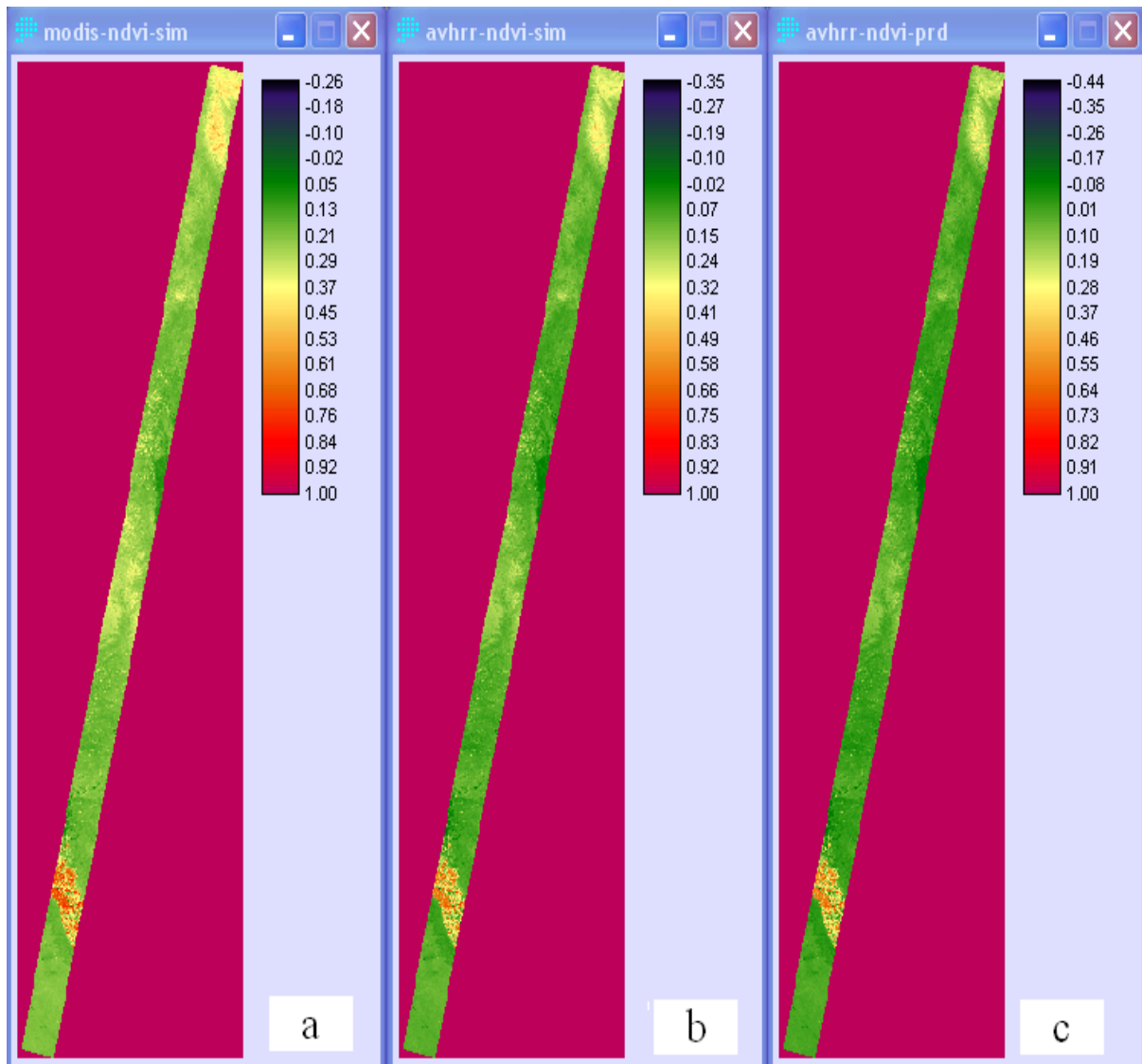


Fig. 5.6. NDVI values calculated from: (a) the simulated MODIS channels, (b) the simulated AVHRR channels calculated directly from Hyperion spectra and (c) the predicted AVHRR channels from the MODIS green, red, NIR and water vapor absorption channels, New Mexico, 19-07-2007.

Now the results of some basic statistical analysis on the images of simulated/predicted channels or NDVI images on 19 July 2007 are represented.

Fig.5.7 shows the frequency distribution of the calculated apparent reflectance values for the directly simulated AVHRR and MODIS red channels from Hyperion spectra for all pixels in the entire scene. The mean apparent reflectances of the AVHRR red and MODIS red channels are 0.2053 and 0.2143, respectively. The mean apparent reflectance of the AVHRR red channel is smaller than that of the MODIS red channel by about 0.0090 because the AVHRR red channel covers larger wavelength region with lower reflectance (c.f. fig. 4.2).

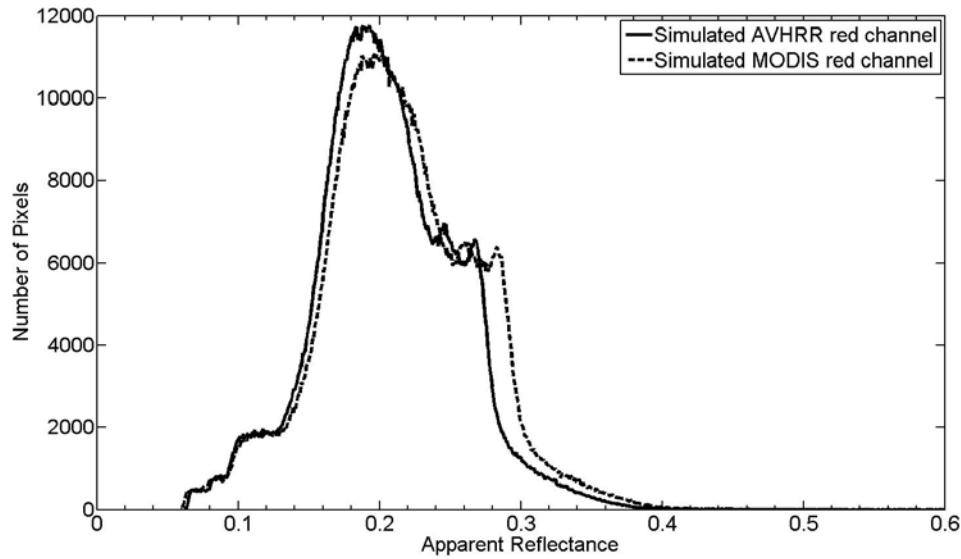


Fig.5.7. Histograms of the calculated apparent reflectance values for the directly simulated AVHRR red and MODIS red channels from Hyperion spectra for all pixels in the entire scene, New Mexico, 19-07-2007.

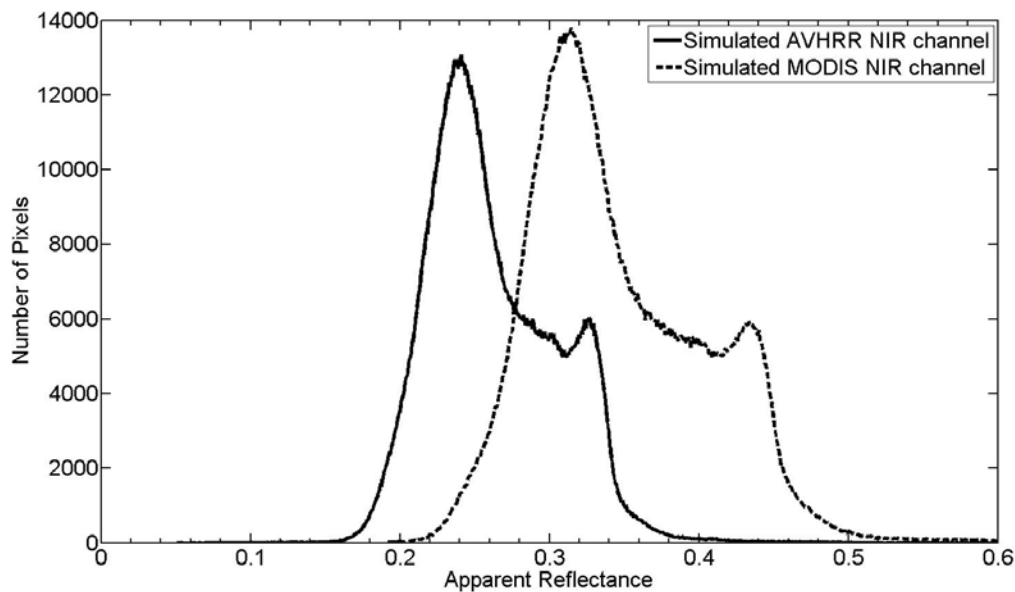


Fig.5.8. Histograms of the calculated apparent reflectance values for the directly simulated AVHRR and MODIS NIR channels from the Hyperion spectra for all pixels in the entire scene, New Mexico, 19-07-2007.

Histograms of the calculated apparent reflectance values for the directly simulated AVHRR and MODIS NIR channels from the Hyperion spectra for all pixels in the entire scene are shown in fig. 5.8. The mean apparent reflectance of the AVHRR and MODIS NIR channels are 0.2626 and 0.3467 (reflectance unit), respectively. The mean apparent reflectance of the AVHRR NIR channel is smaller than that of the MODIS channel by about 0.0841 because the AVHRR NIR channel covers larger wavelength region with lower reflectance mainly due to strong water vapor absorption effects in the bandpass of the AVHRR NIR channel (see fig.

4.2). It is expected to have large bias between NDVI values derived from the simulated AVHRR and MODIS channels because of this large difference in the mean reflectance values in their NIR channels.

Histograms of the NDVI values calculated from the directly simulated AVHRR and MODIS channels in the entire scene are shown in fig.5.9. On average, the AVHRR and MODIS NDVI values are 0.1293 and 0.2419 (shown by vertical hatched lines), respectively. This fact that mean NDVI values are low reveals that there is sparse vegetation in the area. The lower mean NDVI value derived from the simulated AVHRR channels compared with that from the simulated MODIS channels can be because of lower mean apparent reflectance of the AVHRR NIR channel compared to mean apparent reflectance of the simulated MODIS NIR channel (c.f. fig.5.8). The difference in the mean NDVI values indicates that there is bias of 0.1126 in the AVHRR NDVI estimation using the simulated MODIS red and NIR channels.

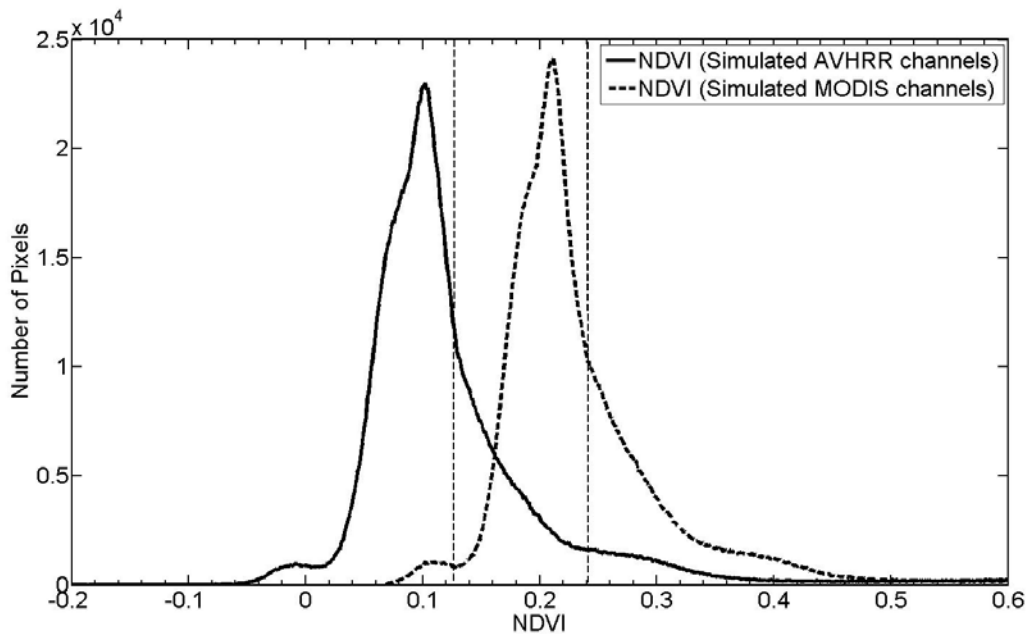


Fig.5.9. Histograms of the NDVI values derived from the directly simulated AVHRR and MODIS channels for the entire scene, New Mexico, 19-07-2007. Vertical hatched lines indicate the mean of NDVI values in the entire scene.

Fig.5.10 represents histogram of the simulated AVHRR red in apparent reflectance values calculated directly from the Hyperion spectra via simple averaging and the histogram of the predicted AVHRR red channel using directly simulated MODIS green and red channels in the equation (3) for all pixels in the entire scene. The small difference between the mean apparent reflectance values of the simulated and the predicted AVHRR red channels (about 0.0039 in reflectance unit) demonstrates that AVHRR red channel can be predicted almost well using simulated MODIS green and red channels.

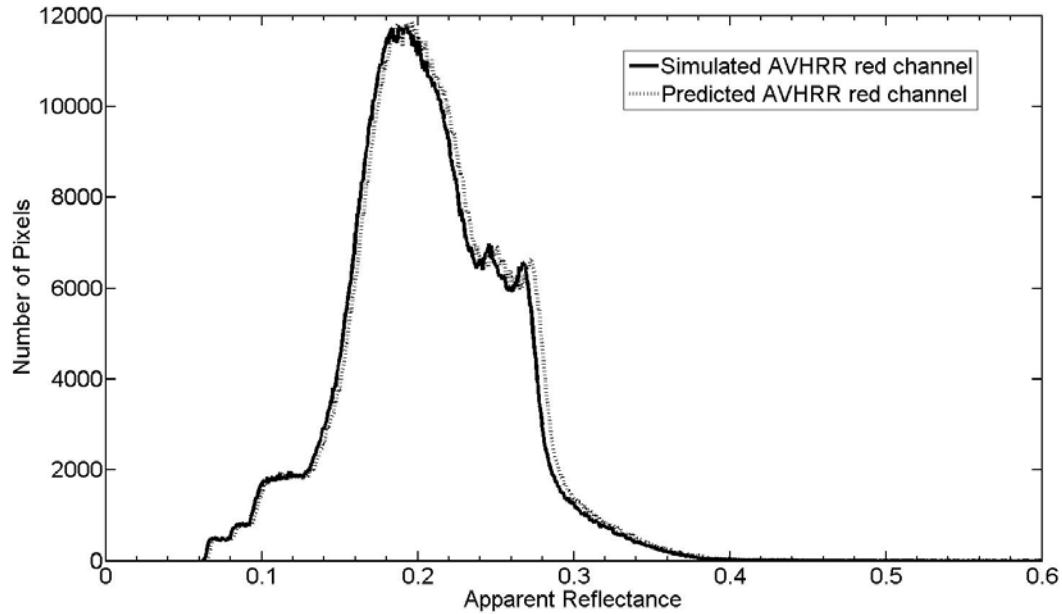


Fig.5.10. Histogram of the calculated apparent reflectance values for the directly simulated AVHRR red channel from Hyperion spectra and the histogram of the predicted AVHRR red channel in reflectance values from directly simulated MODIS green and red channels for all pixels in the entire scene, New Mexico, 19-07-2007.

Histogram of the calculated apparent reflectance values for the directly simulated AVHRR NIR channel from Hyperion channels is plotted in fig. 5.11. This figure also includes the histogram of the predicted AVHRR NIR channel from the directly simulated MODIS NIR and water vapor absorption channels for all pixels in the entire scene. The mean apparent reflectance values of the simulated and predicted AVHRR NIR channels are 0.2626 and 0.2266 in reflectance unit, respectively. On average, the difference between the simulated AVHRR NIR channel and the predicted channel (0.0360) is less than the difference between the simulated AVHRR NIR channel and the simulated MODIS NIR channel (0.1126) shown in fig. 5.8.

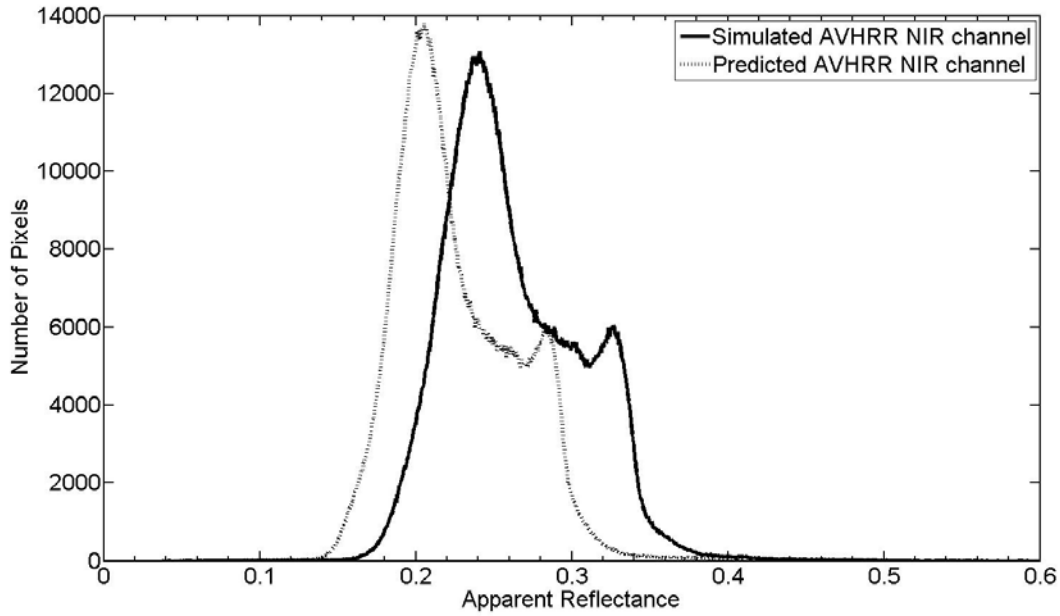


Fig.5.11. Histogram of the calculated apparent reflectance values for the directly simulated AVHRR NIR channel from the Hyperion spectra and the histogram of the predicted AVHRR NIR channel in reflectance values from the directly simulated MODIS NIR and water vapor absorption channels in the entire scene, New Mexico, 19-07-2007.

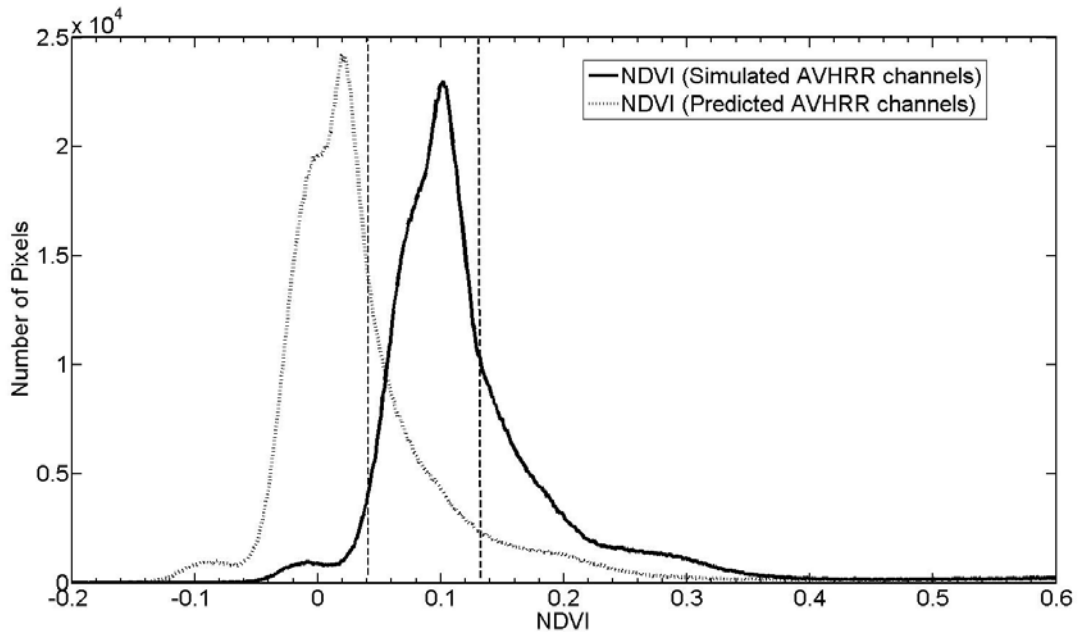


Fig.5.12. Histogram of the AVHRR NDVI values calculated from the simulated AVHRR channels through averaging Hyperion spectra and histogram of the predicted AVHRR NDVI values calculated from the AVHRR channels predicted with MODIS green, red, NIR and water vapor absorption channels in the entire scene, New Mexico, 19-07-2007. Vertical hatched lines show the place of mean NDVI values on the horizontal axis.

Histogram of the AVHRR NDVI values calculated from the directly simulated AVHRR channels and histogram of the AVHRR NDVI values calculated from the AVHRR channels

(predicted with MODIS green, red, NIR and water vapor absorption channels) in the entire scene are compared visually in fig.5.12. Vertical hatched lines indicate the mean values of the simulated AVHRR NDVI and the predicted AVHRR NDVI (0.1293 and 0.0469, respectively).

Histograms and mean values (vertical hatched lines) of the simulated AVHRR NDVI, predicted AVHRR NDVI and simulated MODIS NDVI images are compared in fig. 5.13. It can be seen that the difference between the mean of the simulated AVHRR NDVI values and the mean of predicted AVHRR NDVI values (0.0824 in fig.5.12) is smaller than the difference between the mean of the simulated AVHRR NDVI values and the mean of the simulated MODIS NDVI values (0.1126 in fig. 5.9). Thus, the presented method for the prediction of AVHRR NDVI using four simulated MODIS green, red, NIR and water vapor absorption channels from Hyperion spectra reduces the bias in the prediction of AVHRR NDVI estimates by 27% compared to the case when it is estimated with simulated MODIS NDVI.

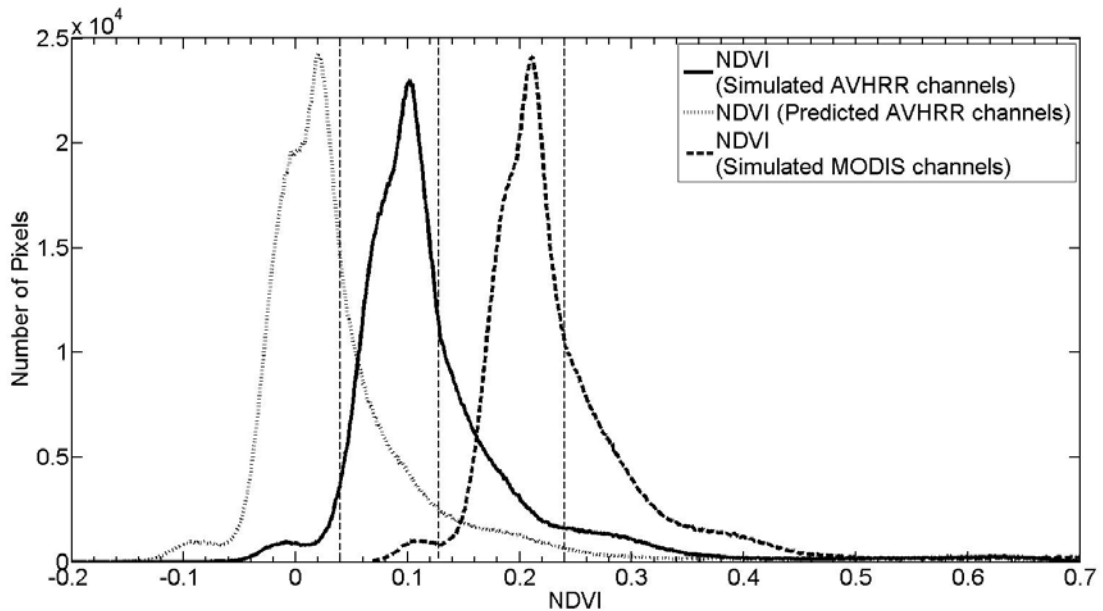


Fig.5.13. Histogram of the simulated AVHRR NDVI values calculated from the simulated AVHRR channels, histogram of the predicted AVHRR NDVI values derived from MODIS green, red, NIR and water vapor absorption channels and histogram of the simulated MODIS NDVI values calculated from the simulated MODIS channels in the entire scene, New Mexico, 19-07-2007. Vertical hatched lines represent the mean NDVI values.

5.2. Results of the consistency evaluation

Below, the results of the consistency analysis including Pearson correlation and linear regression analysis in the shrubland and grassland sites in 2007 are represented.

The simulated MODIS NDVI time series (down-scaled to 250 m resolution) and the real (Terra and Aqua) values (16-day composites with 250m resolution) for the shrubland site in 2007 are plotted in fig. 5.14. Fig. 5.15 shows the same time series for the grassland site in 2007. In both figures (5.14 and 5.15) the number of simulated values (15) is lower than the number of real values (23) and time step of the simulated MODIS NDVI time series is changed during the year because of disordered temporal resolution of the Hyperion data (see table 3.3). In both sites, the simulated NDVI values are lower than the real values in entire the year. In addition, the simulated NDVI values are closer to real MODIS/Terra NDVI values than the MODIS/Aqua in the grassland site (fig. 5.15). This can be because of small time difference in the equatorial crossing time for the MODIS/Terra and Hyperion platforms (see table 3.1)

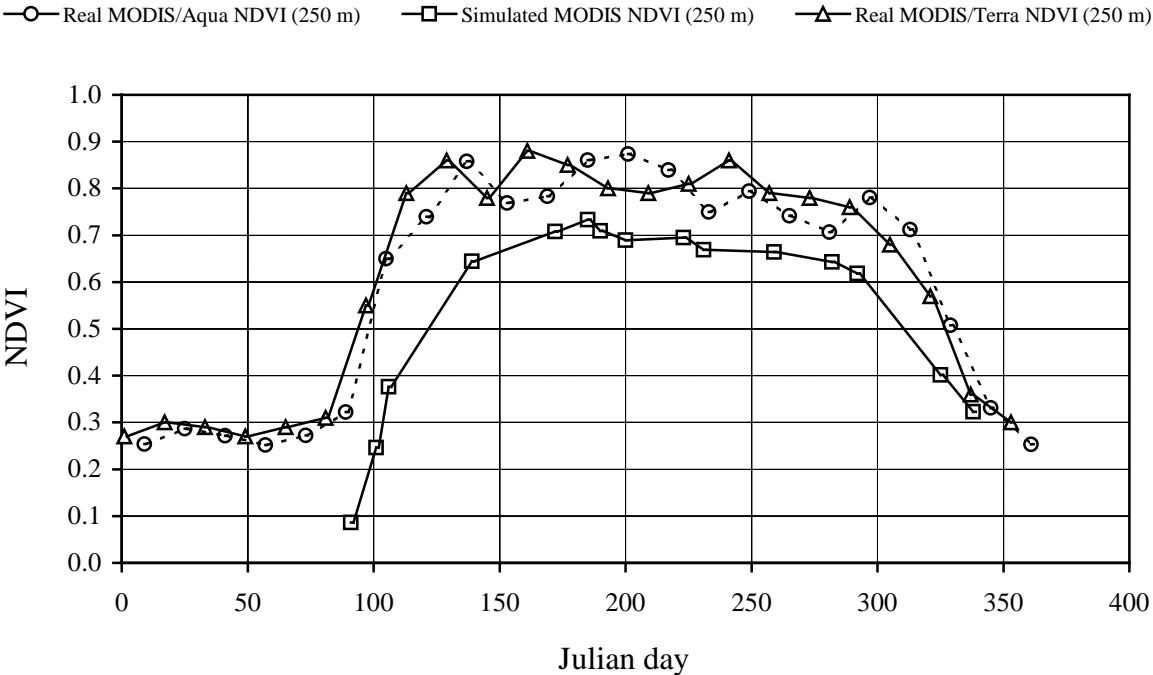


Fig.5.14. The simulated and the real MODIS (Terra & Aqua) NDVI time series (250 m) in the shrubland site in 2007. ($N_{real} = 23$, $N_{simulated} = 15$)

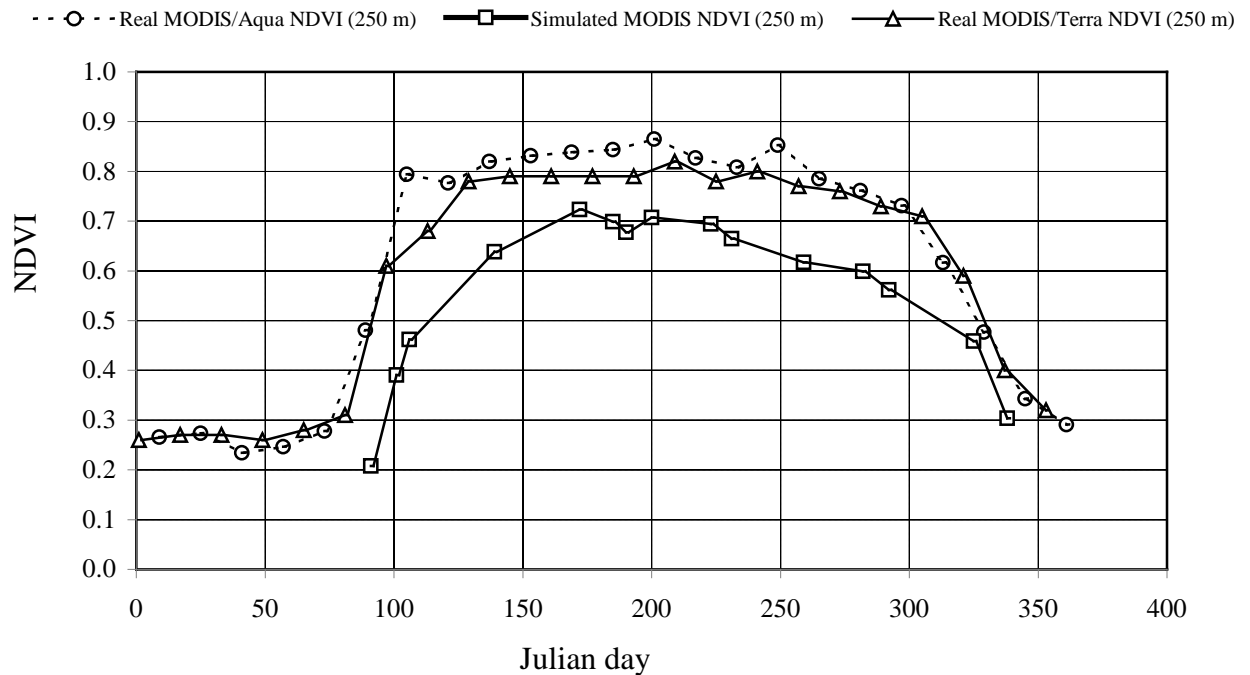


Fig. 5.15. The simulated and the real MODIS (Terra & Aqua) NDVI time series (250 m) in the grassland site in 2007. ($N_{real} = 23$, $N_{simulated} = 15$)

Crossplots of the simulated MODIS NDVI against the real MODIS/Aqua and MODIS/Terra NDVI time series (250 m) in the shrubland site in 2007 are shown in the fig. 5.16, subfigures *a* and *b* respectively. The simulated values are highly correlated with the real NDVI values, MODIS/Terra slightly more than MODIS/Aqua (0.97 and 0.84, respectively) especially in the low NDVI region. P-values of the correlation coefficients (0.0002 and 0.0001) are less than 0.05, meaning that the correlation coefficients are significant at 95% confidence interval. Additionally, the RMSE (obtained by equation 6) of the simulated values and the MODIS/Terra values (0.15 ndvi unit) is lower than that with the MODIS/Aqua (0.19 ndvi unit). Regression equations between the simulated and the real values are shown inside the boxes over the fig 5.16. The regression coefficients (0.74 and 0.93) are significant at the 95% significant level and that between the simulated MODIS NDVI and the real MODIS/Terra (0.93) is higher than the coefficient with MODIS/Aqua (0.74).

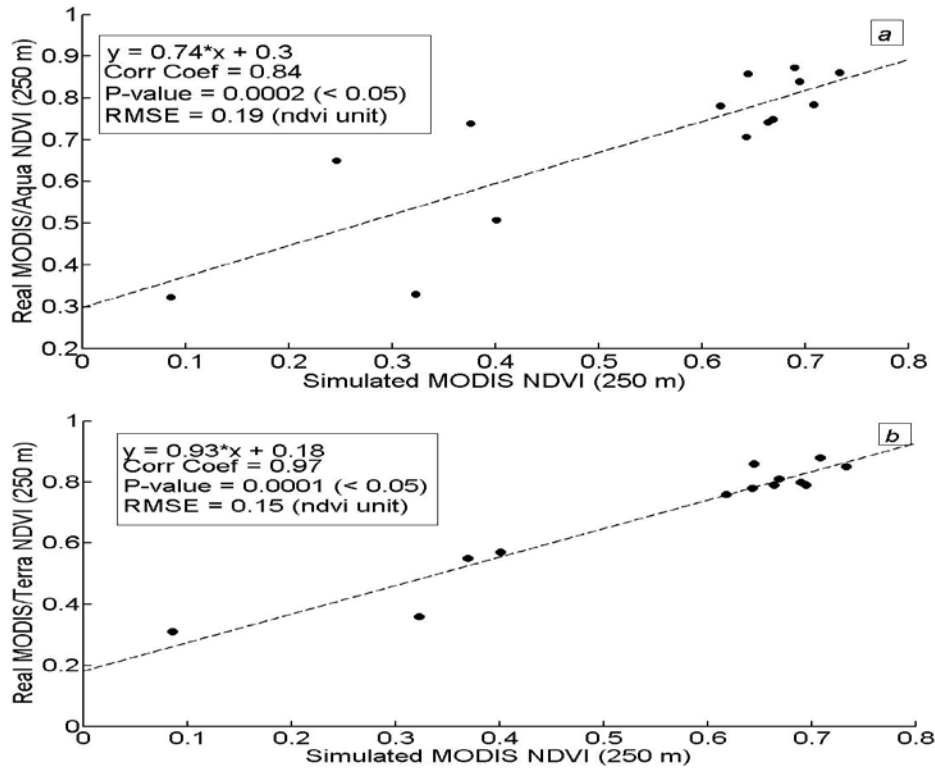


Fig. 5.16. Correlation and linear regression analysis between the (a): simulated and real MODIS/Aqua NDVI (b): simulated and real MODIS/Terra NDVI time series (250 m) in the shrubland site in 2007. (x = horizontal axis, y =vertical axis, $N_a = 14$, $N_b = 13$)

The same correlation and linear regression analysis is performed for the grassland site. Fig. 5.17 shows the crossplot of the simulated and the real MODIS/Aqua and MODIS/Terra NDVI time series, subfigures *a* and *b*, in the grassland site in 2007. In this site there is almost the same statistics like shrubland site: the simulated and real NDVI values are strongly correlated and the correlation coefficient between the simulated values and MODIS/Terra (0.98) is higher than that with MODIS/Aqua (0.81). The p-values (0.0004 and 0.0001) less than 0.05 confirm the significance of the correlation coefficients. The RMSE of the simulated and the real MODIS/Terra NDVI values (0.13 ndvi unit) is lower than that of MODIS/Aqua (0.20 ndvi unit).

The linear regression equations between the simulated and the real MODIS (Aqua and Terra) NDVI values are represented inside the boxes in up left corners of the subfigures *a* and *b* in fig.5.17. The regression coefficient with MODIS/Terra is more than that with MODIS/Aqua, 0.99 and 0.82 respectively.

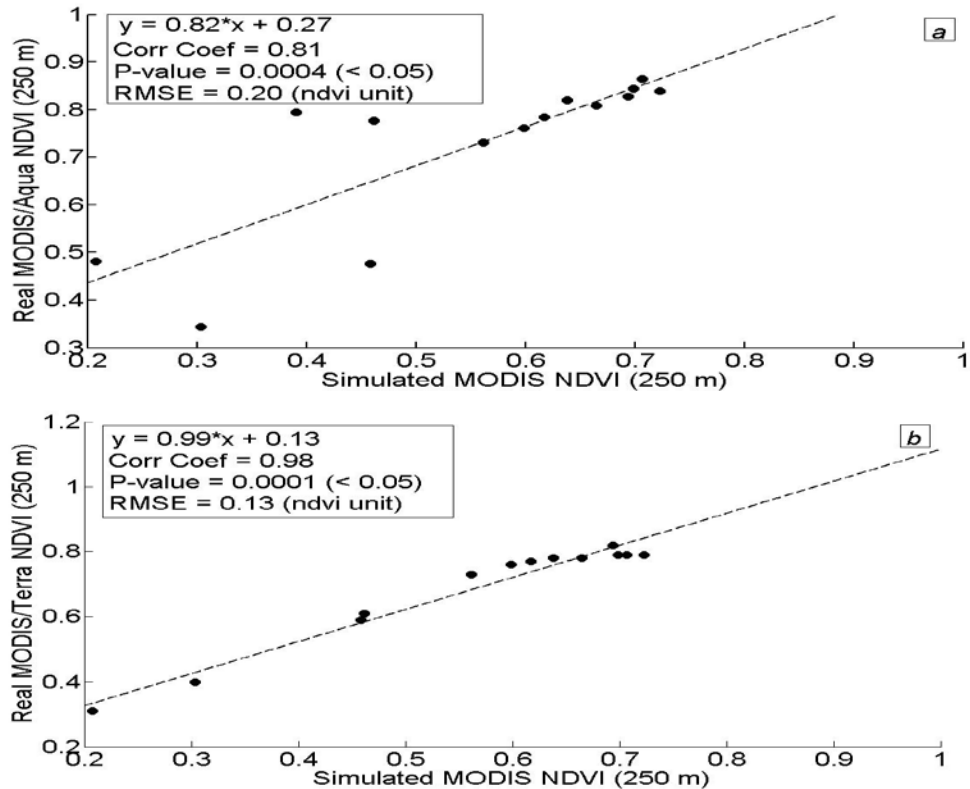


Fig. 5.17. Correlation and linear regression analysis between the (a): simulated and real MODIS/Aqua NDVI (b): simulated and real MODIS/Terra NDVI time series (250 m) in the grassland site in 2007. (x = horizontal axis, y =vertical axis, $N_a=14$, $N_b=13$)

In the correlation computations, it is noted that the real MODIS NDVI values have been measured for every 16 days with the beginning on the Julian days 1 for Aqua/MYD13Q1 product and 9 for Terra/MOD13Q1 product (see Appendix F). But, the simulated MODIS NDVI values are disordered in time step. Thus, in correlation analysis when the simulated and the real values are not available at the same day, the day of the simulated NDVI values for each site is changed with the nearest day within those 16 days for which the real MODIS NDVI has been measured. This date change does not decrease the correlation coefficients precision because of the fact that Hyperion data and consequently the simulated MODIS NDVI are assigned for a specific day (satellite image acquiring day) and this day is one of those 16 days that the real MODIS NDVI data are measured. If more than one simulated value are within the corresponding 16-day of real values averaged value of the simulated values is considered in the correlation analysis and the number of simulated values is decreased (compare the number of points in fig. 5.17 and fig. 5.16 with those in fig. 5.14 and fig. 5.15)

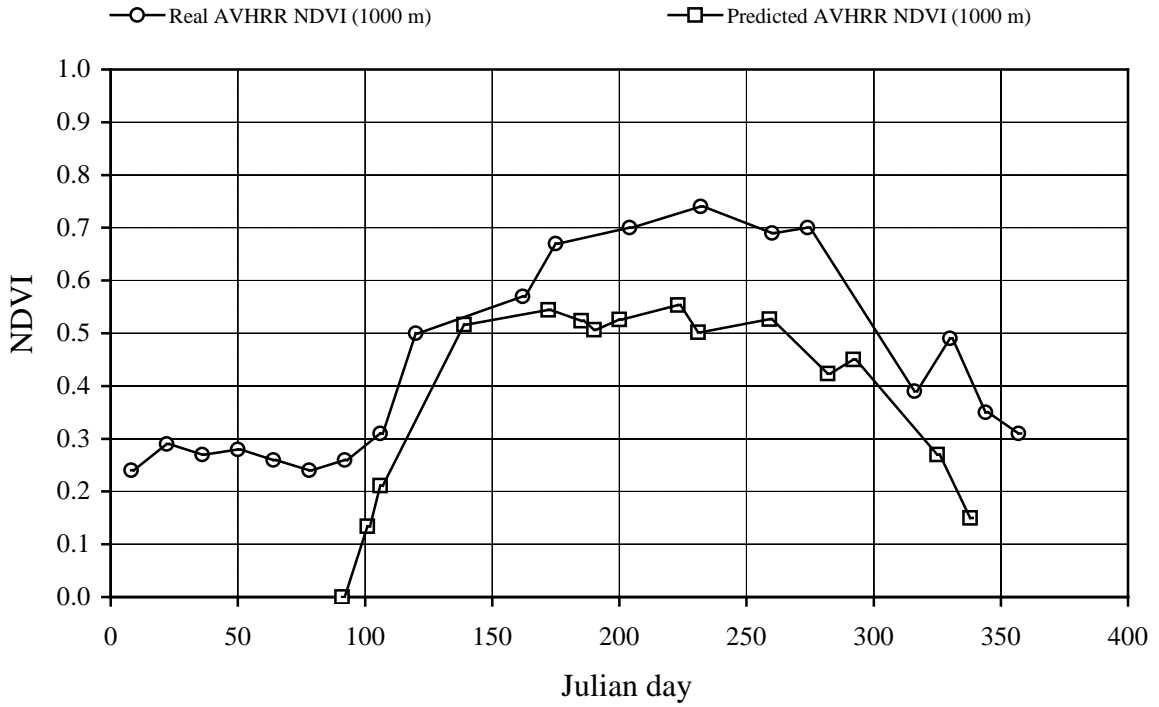


Fig. 5.18. The real and the predicted AVHRR NDVI (1000 m) in the shrubland site in 2007. ($N_{real} = 19$, $N_{simulated} = 15$)

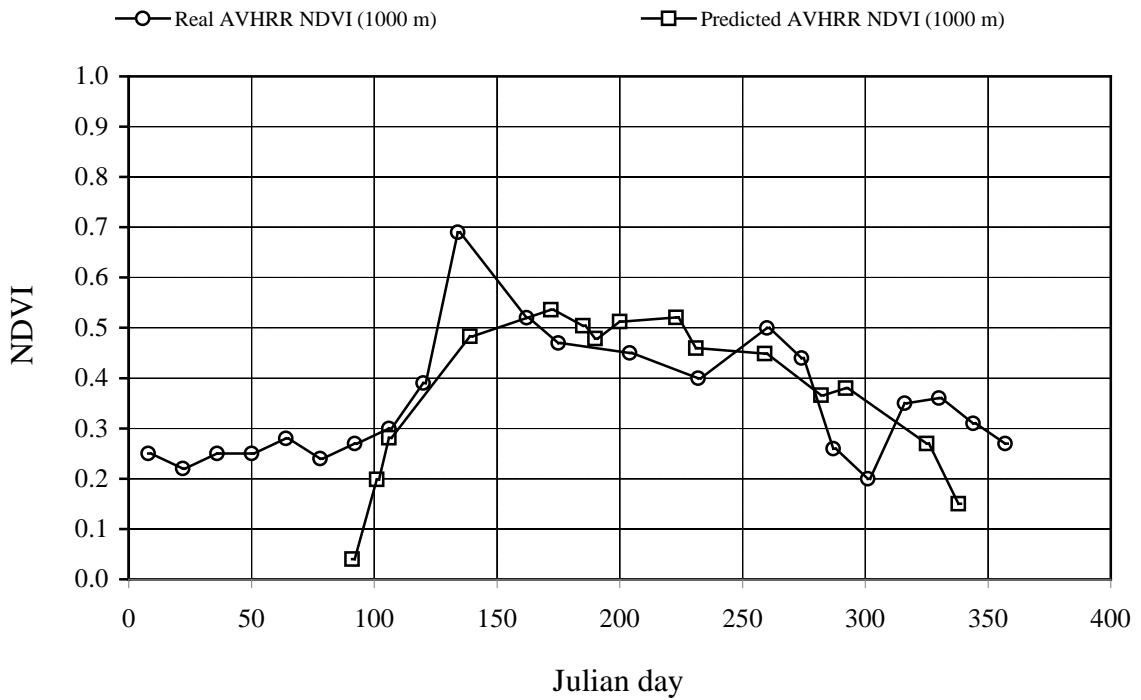


Fig. 5.19. The real and the predicted AVHRR NDVI (1000 m) in the grassland site in 2007. ($N_{real} = 22$, $N_{simulated} = 15$)

The real and the predicted AVHRR NDVI time series (using Hyperion data) for the shrubland and grassland sites in 2007 are shown in fig. 5.18 and fig. 5.19, respectively. The real AVHRR NDVI are biweekly composites (beginning on the Julian day 8, see Appendix F) while the predicted values are in the specific days (satellite image acquiring day, see table 3.3). A few of the real AVHRR NDVI values in both sites are not considered in the analysis due to cloud effects. The real values have originally 1000 m spatial resolution and the predicted values have been already downsampled from 30 m to 1000 m.

In shrubland site (fig. 5.18), predicted values are lower than the real values in entire the year but in the grassland site (fig. 5.19) the predicted values are almost higher than the real values in the high NDVI region. Shrubland site has almost higher NDVI values compared to the grassland site.

Crossplots of the real and the predicted AVHRR NDVI values for the shrubland and grassland sites in 2007 are plotted in fig 5.20 and 5.21, respectively. In the correlation coefficients computations, the days of the predicted AVHRR NDVI values is set to the nearest day of the real values within corresponding 14 days in which they have been measured.

Pearson correlation coefficients, between the real and the predicted AVHRR NDVI values at 1000 m spatial resolution in the shrubland site and grasslands are 0.87 and 0.66, respectively. Low p-values (less than 0.05) in both sites indicate that the correlation coefficients are significant at 95% significant level. The grassland site has lower RMSE than the shrubland site by 0.06-ndvi unit. With comparing the regression equations (shown inside the boxes on the subfigure) between the predicted and the real AVHRR NDVI in the sites, it is seen that the regression coefficient in the shrubland site is higher than that in the grassland site, 0.87 and 0.61 respectively.

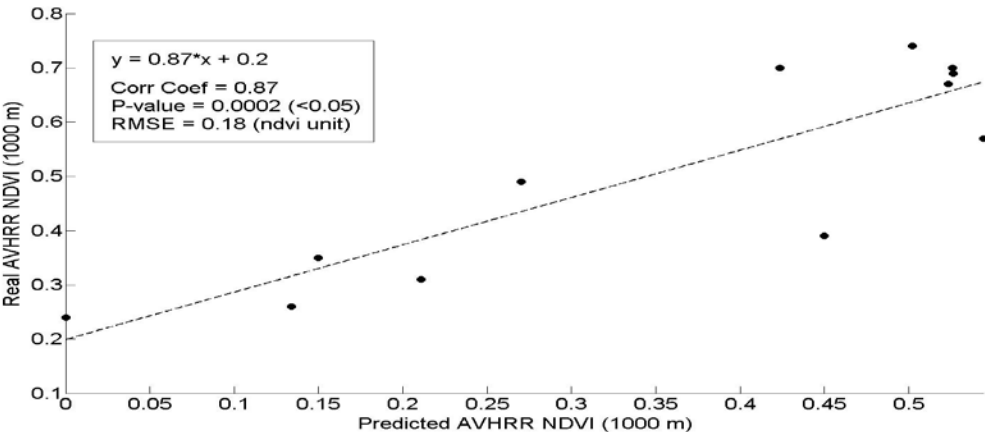


Fig. 5.20. Correlation and regression analysis between the real and the predicted AVHRR NDVI (1000 m) in the shrubland site in 2007. (x=horizontal axis, y=vertical axis, N =12)

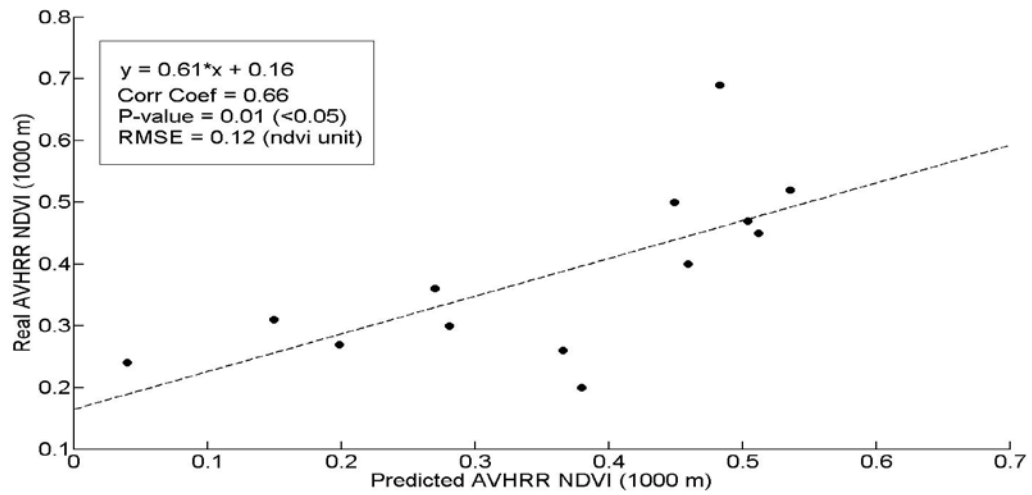


Fig. 5.21. Correlation and regression analysis between the real and the predicted AVHRR NDVI (1000 m) in the grassland site in 2007. (x= horizontal axis, y=vertical axis, N =13)

Chapter 6: Discussion and Conclusion

6.1. Discussion

The tested method based on the Hyperion data and MODO software is able to simulate the MODIS NDVI and to predict the AVHRR NDVI with a good spatial resolution (30 m) in the study area (a semi-arid region).

In this method, the simulated MODIS red and NIR channels (30 m resolution) are close by 0.0090 and 0.0841 reflectance-unit to the simulated AVHRR channels, respectively (see fig. 5.7 and 5.8). Miura et al. (2006) derived the ranges of -0.01 to 0.016 for the red and 0.0 to 0.033 for the NIR channels as the reflectance differences between the simulated MODIS and AVHRR channels over a tropical-savanna transitional region in Brazil. They used one Hyperion image of the area. It was corrected for atmosphere effects with the '6S' radiative transfer code to retrieve the ground reflectances.

Since there is no significant gaseous atmospheric effect on the AVHRR red channel (see fig. 4.2) this channel is predicted accurately (0.0039 reflectance unit in fig. 5.10) using the simulated MODIS red and green channels in the tested method. This difference is comparable with the results reported by Bo-Cai (2000) (0.002 to 0.005 depending on the humid or dry atmosphere conditions, respectively). It is demonstrated that MODO transfer code has this capability to handle the most difficulty in the prediction of AVHRR NIR channel, which is because of the atmospheric absorption effects, by reducing the bias between simulated and predicted NIR channels to the 0.0360-reflectance unit (c.f. fig. 5.11). Remained uncertainties in the predicted AVHRR channels make the predicted AVHRR NDVI values to be biased by about 0.0824-ndvi unit compared to the simulated AVHRR NDVI values. This bias is still lower than the bias between the simulated MODIS NDVI and the simulated AVHRR NDVI (0.1126-ndvi unit in fig. 5.9) indicating that the tested method can predict the AVHRR NDVI (30 resolution) by about 0.27-ndvi unit lower bias compared to the case when it is computed only by using the simulated MODIS NDVI channels.

In the NDVI time series analysis, simulated MODIS NDVI values (250 m) are lower than the real values in both shrubland and grassland sites in 2007 (see fig. 5.14 and 5.15). Simulated values have strong correlation (more than 0.80) with the real MODIS NDVI values in both shrubland and grassland sites (see fig. 5.16 and 5.17). Correlation with MODIS/Terra is higher than MODIS/Aqua. RMSE of the simulated MODIS NDVI is in the range of 0.13 to 0.20 ndvi-unit in both sites. This means that it is possible to obtain the simulated MODIS NDVI in a 30 m resolution without using MODO or any other code for the atmospheric corrections. There is lower RMSE with MODIS/Terra compared to the MODIS/Aqua (see fig. 5.16 and 5.17). Better results in terms of higher positive correlation and lower RMSE with MODIS/Terra indicate that simulated MODIS NDVI can model the Terra NDVI better than Aqua NDVI. This can be because of the close equatorial crossing times of Terra and Hyperion platforms (see table 3.1). The simulated MODIS NDVI values are slightly more consistent

with MODIS/Terra NDVI values in the grassland site than in the shrubland site (see subfigures *b* in the fig 5.16 and 5.17).

Predicted AVHRR NDVI (rescaled to 1000 m resolution) values are lower than the real values in 2007 in the grassland site while it is not the case in the shrubland site where in some dates the predicted values are higher than the real values (see fig. 5.18 and 5.19). Thus it can be said that the bias between the predicted and the real values is changed with the land covers and vegetation density, which is in agreement with the report of Jonas and Menz (2004).

In the grassland site, there is less correlation between the predicted and real AVHRR NDVI values compared to the shrubland site (0.66 and 0.87, respectively) whereas grassland site has lower RMSE by about 0.06 ndvi-unit (see fig 5.20 and 5.21).

For easier comparison, the results of the correlation and regression analysis shown inside the boxes in the fig. 5.16, 5.17, 5.20 and 5.21 are represented again all together in Table 6.1.

By comparing the results of the consistency evaluation in the grassland and shrubland sites (table 6.1), it is seen that the simulated MODIS NDVI have the highest consistency (low RMSE and high correlation) with the real MODIS/Terra values. The predicted AVHRR NDVI has the second rank in consistency following by the MODIS/Aqua NDVI as the last one with the lowest consistency. The RMSE values either for MODIS/Terra NDVI or AVHRR NDVI datasets are lower in the grassland site than the shrubland site.

Table 6.1. Results of the consistency evaluation analysis in the shrubland and grassland sites in 2007. (extracted from fig. 5.16, 5.17, 5.20 and 5.21)

Datasets	Pearson correlation coefficient		RMSE (ndvi unit)	
	Shrubland site	Grassland site	Shrubland site	Grassland site
Real and simulated MODIS/Aqua NDVI	0.84	0.81	0.19	0.20
Real and simulated MODIS/Terra NDVI	0.97	0.98	0.15	0.13
Real and predicted AVHRR NDVI	0.87	0.66	0.18	0.12

From input-output comparison standpoint, it can be said that any advantages or limitations in the input data (here Hyperion) are transferred directly to the output results in the tested method. For instance, the geographical coverage areas, spatial and temporal resolutions of the simulated/predicted NDVI images are exactly the same as the input data. High spatial resolution of the Hyperion imagery (30 m) can be a positive criterion for the simulated NDVI imagery while weak temporal resolution (i.e., disordered time steps) and its small coverage (7.5 km×100 km) compared to the covered area by a real AVHRR NDVI image (often globe

coverage) can make some lacks in the providing ordered NDVI time series or in the large area applications even though it is possible to order Hyperion images acquisition for the specific times and locations via Hyperion website.

6.2. Source of errors and possible improvements

- In this study, the mean atmospheric gaseous transmittance of all the pixels is used for prediction of the AVHRR NIR channel, but in reality the transmittance spectra are different for different pixels due to the changing water vapor amounts over the pixels. If a radiative transfer code could perform the computations of the atmospheric gaseous transmittances for all pixels within an image, then results of the predicted AVHRR NDVI could be improved.
- The process of down-scaling of simulated/predicted NDVI imagery from 30 m to 250m/1000m can carry some uncertainties due to the geo-location fitting and re-sampling issues. Perhaps, comparing the simulated NDVI values with in-situ measurements which have the same resolution, can make more reliable results in the NDVI consistency evaluations.
- In comparing NDVI values derived from multiple sensors, the atmospheric state and correction methods, sensors geo-location, satellite and sun geometries, NDVI composing techniques are of great importance and can shift NDVI values (Van Leeuwen et al., 2006).

6.3. Conclusion

From this study, following are concluded:

- The tested method using Hyperion imagery and MODO software can simulate/predict consistent MODIS NDVI (Terra better than Aqua) and AVHRR NDVI in the New Mexico semi-arid region in which the simulated/predicted values have acceptable RMSE (0.12-20 in ndvi unit) and high correlation (0.66-0.98) with the real values.
- However, disordered temporal resolution, existence of a few not-calibrated channels and local coverage of the Hyperion images make some limitations in making a reliable time series for integrating with real AVHRR NDVI time series.
- Atmospheric gaseous impacts particularly Oxygen and water vapor absorption effects on the AVHRR NIR channel are reduced by using MODO software quite well.

6.4. Recommendations

In future studies, for making a more reliable NDVI time series via integration of the predicted and the real AVHRR NDVI data sets it is recommended to use hyper spectral data with higher temporal resolution than the Hyperion data, if there is any. Examining the cross-sensor

relationships of the predicted AVHRR NDVI vs. simulated MODIS NDVI and land cover dependencies of the relationships may reveal interesting points.

References

- Batra, N., Islam, S., Venturini, V., Bisht, G., and Jiang, L., 2006, Estimation and comparison of evapotranspiration from MODIS and AVHRR sensors for clear sky days over the Southern Great Plains: *Remote Sensing of Environment*, v. 103, p. 1-15.
- Be Dard, F., Crump, S., Gaudreau, J., 2006, A comparison between Terra MODIS and NOAA AVHRR NDVI satellite image composites for the monitoring of natural grassland conditions in Alberta, Canada: *Canadian Journal of Remote Sensing*, v. 32, p. 44–50.
- Bo-Cai, G., 2000, A practical method for simulating AVHRR-consistent NDVI data series using narrow MODIS channels in the 0.5-1.0 μm spectral range: *Geoscience and Remote Sensing, IEEE Transactions on*, v. 38, p. 1969-1975.
- Brown, M.E., Lary, D.J., Vrieling, A., Stathakis, D., and Mussa, H., 2008, Neural networks as a tool for constructing continuous NDVI time series from AVHRR and MODIS: *International Journal of Remote Sensing*, v. 29, p. 7141-7158.
- Brown, M.E., Pinzon, J.E., Didan, K., Morisette, J.T., and Tucker, C.J., 2006, Evaluation of the Consistency of Long-Term NDVI Time Series Derived From AVHRR, SPOT-Vegetation, SeaWiFS, MODIS, and Landsat ETM+ Sensors: *IEEE Transactions on Geoscience and Remote Sensing*, v. 44, p. 1787-1793.
- Buheasier, Tsuchiya, K., Kaneko, M., and Sung, S.J., 2003, Comparison of image data acquired with AVHRR, MODIS, ETM and ASTER over Hokkaido, Japan: *Advances in Space Research*, v. 32, p. 2211-2216.
- Carlson, T.N., and Ripley, D.A., 1997, On the Relation between NDVI, Fractional Vegetation Cover, and Leaf Area Index: *Remote Sensing of Environment*, v. 62, p. 241-252.
- Deering, D. W., 1978, Rangeland Reflectance Characteristics Measured by Aircraft and Spacecraft Sensors. College Station, TX: Texas A&M Univ. Press, p. 338.
- Eidenshink, J.C., 1992, The 1990 conterminous U.S. AVHRR data set: *Photogrammetric Engineering and Remote Sensing*, v. 58 (6), p. 809-813.
- Fensholt, R., 2004, Earth observation of vegetation status in the Sahelian and Sudanian West Africa: comparison of Terra MODIS and NOAA AVHRR satellite data: *International Journal of Remote Sensing*, v. 25, p. 1641-1659.
- Gallo, K., Ji, L., Reed, et al., 2004, Comparison of MODIS and AVHRR 16-day normalized difference vegetation index composite data: *Geophysical Research Letters*, v. 31, L07502, 4 pp., 2004
- Huete, A., Didan, K., Miura, T., Rodriguez, E.P., Gao, X., and Ferreira, L.G., 2002, Overview of the radiometric and biophysical performance of the MODIS vegetation indices: *Remote Sensing of Environment*, v. 83, p. 195-213.

- Ji, L., Gallo, K., Eidenshink, J.C., and Dwyer, J., 2008, Agreement evaluation of AVHRR and MODIS 16-day composite NDVI data sets: *International Journal of Remote Sensing*, v. 29, p. 4839-4861.
- Jonas, F., Menz, G., 2004, Sensor intercalibration - adjustment of MODISNDVI-to NOAA-AVHRR-NDVI data: *Geoscience and Remote Sensing Symposium*, v. 3, p.1719-1722
- John, A.G., Christopher, B.F., Michael, L.G., Kevin, L.G., Anne, E.H., Geeske, J., and Riccardo, V., 1995, Relationships between NDVI, canopy structure, and photosynthesis in three Californian vegetation types: *Ecological Applications*, v. 5, p. 28-41.
- Kaufman, Y.J., and Gao, B.C., 1992, Remote sensing of water vapor in the near IR from EOS/MODIS: *Geoscience and Remote Sensing, IEEE Transactions on*, v. 30, p. 871-884.
- Kawamura, K., Akiyama, T., Yokota, H.o., Tsutsumi, M., Yasuda, T., Watanabe, O., and Wang, S., 2005, Quantifying grazing intensities using geographic information systems and satellite remote sensing in the Xilingol steppe region, Inner Mongolia, China: *Agriculture, Ecosystems and Environment*, v. 107, p. 83-93.
- Miura, T., Huete, A., and Yoshioka, H., 2006, An empirical investigation of cross-sensor relationships of NDVI and red/near-infrared reflectance using EO-1 Hyperion data: *Remote Sensing of Environment*, v. 100, p. 223-236.
- Pedelty, J., Devadiga, S., Masuoka, E., Brown, M., Pinzon, J., Tucker, C., Roy, D., Junchang, J., Vermote, E., Prince, S., Nagol, J., Justice, C., Schaaf, C., Jicheng, L., Privette, J., and Pinheiro, A., 2007, Generating a long-term land data record from the AVHRR and MODIS Instruments: *IEEE International Geoscience and Remote Sensing Symposium*, p. 1021-1025.
- Steven, M.D., Malthus, T.J., Baret, F., Xu, H., and Chopping, M.J., 2003, Intercalibration of vegetation indices from different sensor systems: *Remote Sensing of Environment*, v. 88, p. 412-422.
- Trishchenko, A.P., Cihlar, J., and Li, Z., 2002, Effects of spectral response function on surface reflectance and NDVI measured with moderate resolution satellite sensors: *Remote Sensing of Environment*, v. 81, p. 1-18.
- Tucker, C.J., 1979, Red and photographic infrared linear combinations for monitoring vegetation: *Remote Sensing of Environment*, v. 8, p. 127-150.
- Tucker, C.J., Pinzon, J.E., and Brown, M.E., 2005, An extended AVHRR 8-km NDVI dataset compatible with MODIS and SPOT vegetation NDVI data: *International Journal of Remote Sensing*, v. 26, p. 4485-4499.
- Tucker, C.J., Vanpraet, C.L., Sharman, M.J., and Van Ittersum, G., 1985, Satellite remote sensing of total herbaceous biomass production in the senegalese sahel: 1980-1984: *Remote Sensing of Environment*, v. 17, p. 233-249.

Van Leeuwen, W.J.D., Orr, B.J., and Marsh, S.E., 2006, Multi-sensor NDVI data continuity: Uncertainties and implications for vegetation monitoring applications: *Remote Sensing of Environment*, v. 100, p. 67-82.

Venturini, V., Bisht, G., Islam, S., and Jiang, L., 2004, Comparison of evaporative fractions estimated from AVHRR and MODIS sensors over South Florida: *Remote Sensing of Environment*, v. 93, p. 77-86.

Appendix

Appendix A.

Brief description about MODO Software Version 3.0¹⁷

MODTRAN is a code provide by Air Force Geophysics Laboratory (AFGL) written in FORTRAN computing language for simulation of imaging spectrometry data as well as for modeling of the signal at the sensor level. MODTRAN is handled with ASCII input files, which are not easily set up and this often makes some misunderstandings or mistakes in the analysis.

MODO (MODTRAN Organizer) is an interface of MODTRAN radiative transfer code. This interface is based on IDL programming language, which has been established as de-facto standard for hyper spectral imaging processing. MODO was implemented by ReSe Application Schälfer under support of Remote Sensing Laboratories (RSL) of the University of Zurich. ReSe Application Schälfer is responsible for maintaining and distributing MODO.

Easy use of MODTRAN by providing a graphical user interface (GUI) for creation and translation of input files as well as working with output files in the same working area is the main goal of MODO. In specific, MODO provides the required input ASCII control files of the type 'tape5' or '.tp5', used for definition of atmosphere and geometry, for setting up MODTRAN runs and subsequently processes the output spectra in terms of extraction, conversion and plotting of the results. Additional functionalities such as sensitivity analysis and convolution of spectra to hyper spectral band characteristics are performed in MODO.

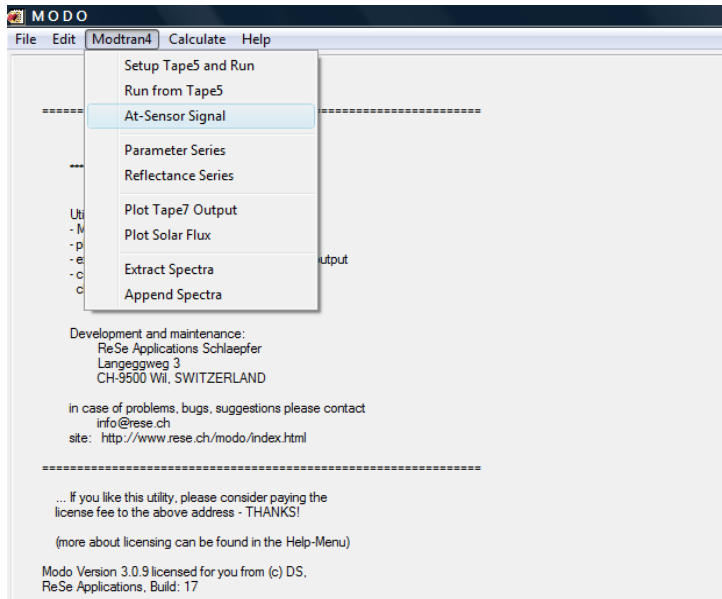
While MODO version 3 used in this study includes different features in terms of dealing with multiple MODTRAN4 tape5 files, editing own atmosphere, supporting for ENVI-TM libraries, extraction of solar flux and transmittance components from MODTRAN output, etc, it is limited to some restrictions such as no support for BRDF functionality of MODTRAN4. In addition MODO version 3 is an expert simulation tool, which still needs the user to be familiar with principles of radiative transfer simulation.

Among different MODO applications, simulation of atmospheric signature has been used in this study. In following a brief description of simulation of atmospheric gaseous (mainly water vapor and Oxygen) transmittance using MODO version 3 is outlined.

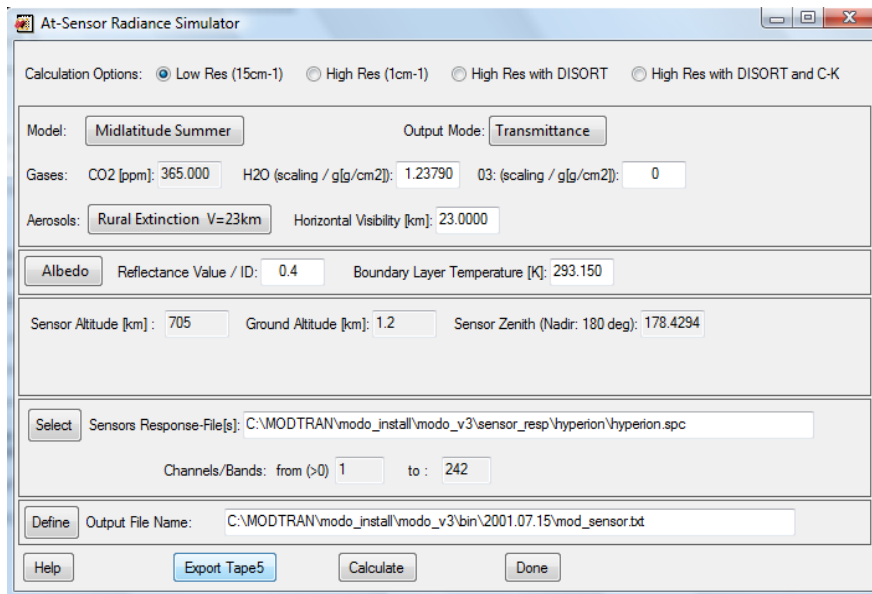
For atmospheric gaseous transmittance simulation the workflow is as below:

¹⁷ Source: MODO USER MANUAL

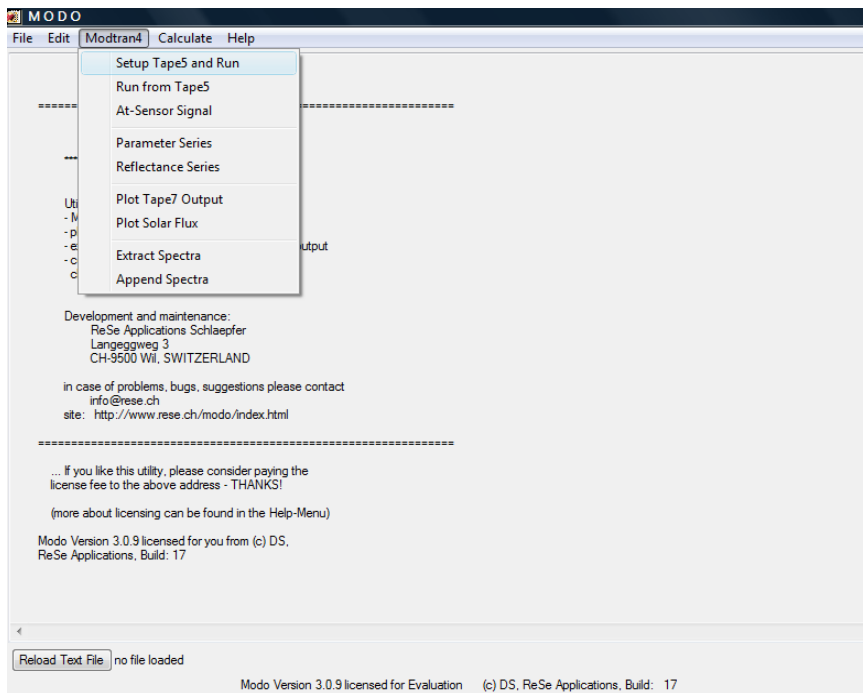
1- Run MODO version3 and choose the path: Modtran4 > At-Sensor Signal



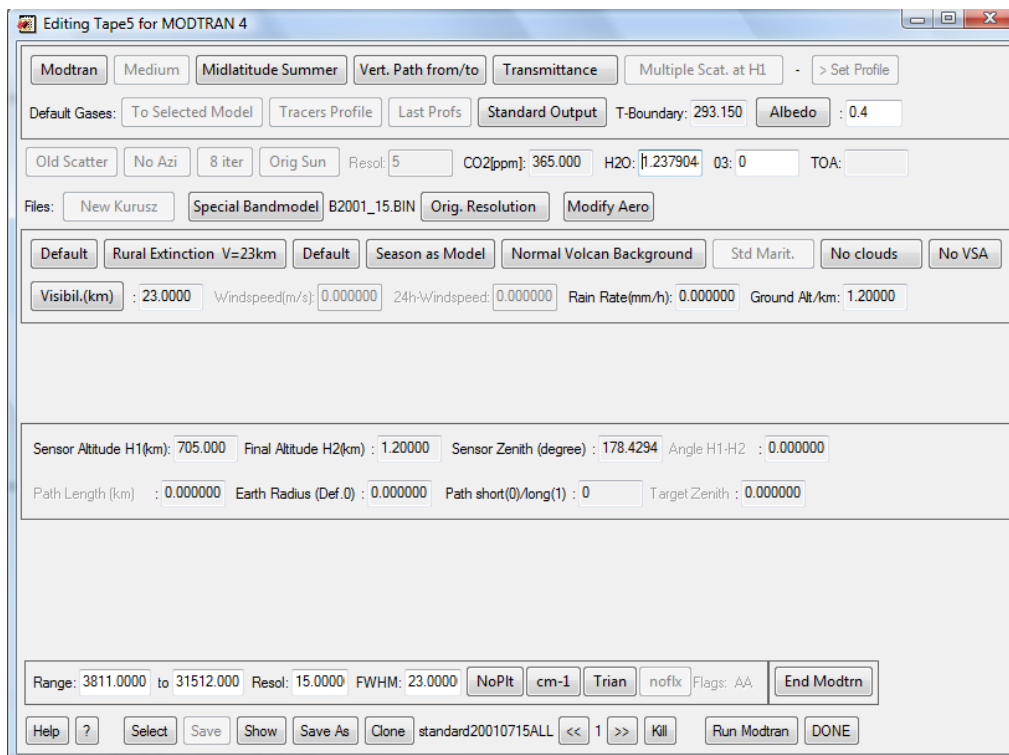
2- Set up At-Sensor simulation parameters like below:



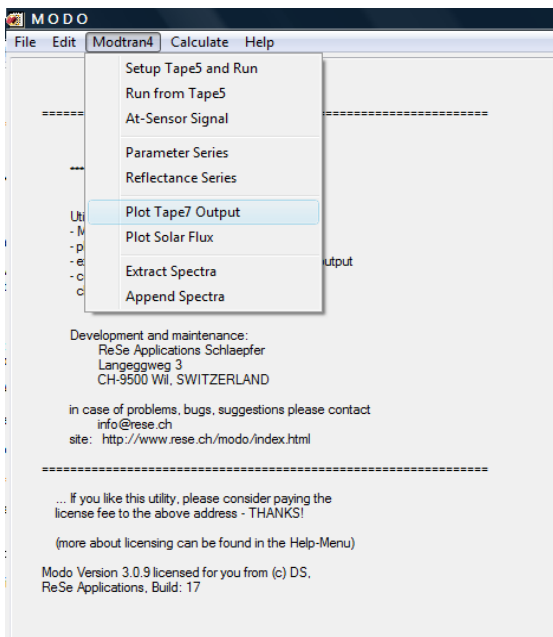
3- Choose the path: Modtran4 > Setup Tape5 and Run



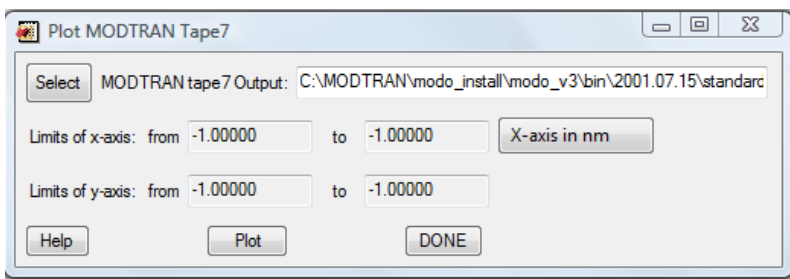
4- Set up Tape5 file parameters and run MODTRAN below:



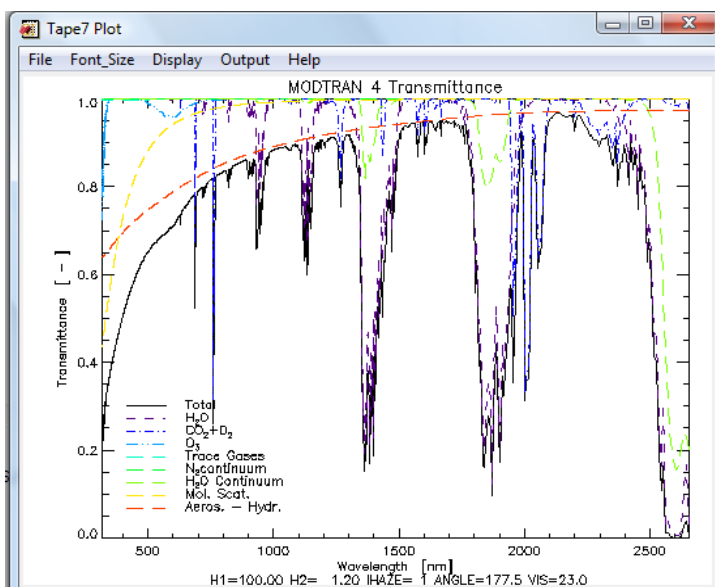
5- Choose the path: Modtran4 > Plot Tape7 Output



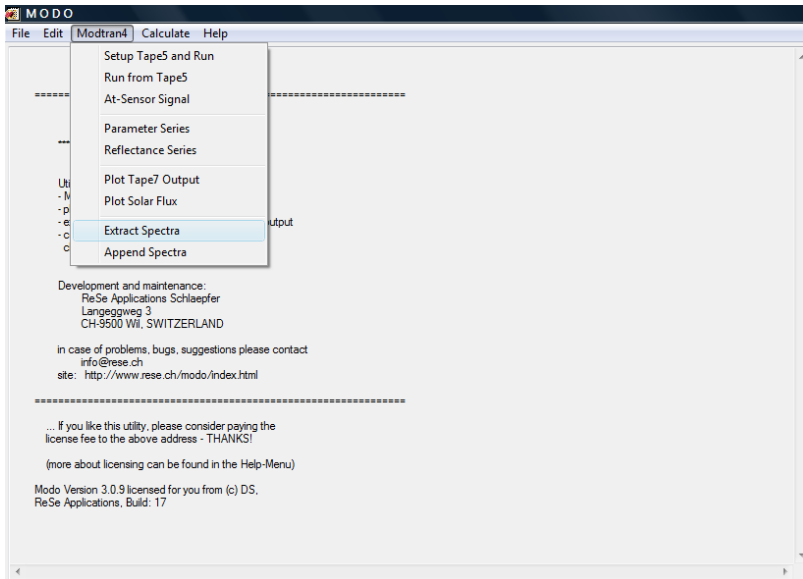
6- Plot MODTRAN output file as below:



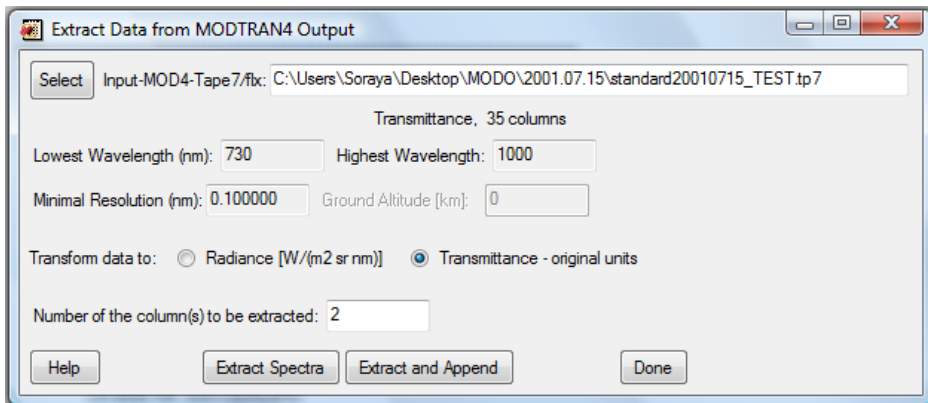
7- Gaseous transmittance spectrum as output is like below:



8- To have particular spectrum choose the path: Modtran4 > Extract Spectra



9- Edit the parameters of specific spectrum as below:



Note: For extraction of water vapor and Oxygen spectrums the numbers of the columns which should be extracted are 2 and 3, respectively.

Appendix B.

HYPERION Spectral details

HYPERION Spectral Coverage						
ALI Band Comparison		Hyperion Band	Average Wavelength (nm)	Full Width at Half the Maximum	Spatial Resolution (m)	Not Calibrated (X)
MS	Pan (nm) 480 - 690 (X)					
		B1	355.5900	11.3871	30	X
		B2	365.7600	11.3871	30	X
		B3	375.9400	11.3871	30	X
		B4	386.1100	11.3871	30	X
		B5	396.2900	11.3871	30	X
		B6	406.4600	11.3871	30	X
		B7	416.6400	11.3871	30	X
		B8	426.8200	11.3871	30	
MS-1		B9	436.9900	11.3871	30	
MS-1		B10	447.1700	11.3871	30	
MS-1'		B11	457.3400	11.3871	30	
MS-1'		B12	467.5200	11.3871	30	
MS-1'		B13	477.6900	11.3871	30	
MS-1'	X	B14	487.8700	11.3784	30	
MS-1'	X	B15	498.0400	11.3538	30	
MS-1'	X	B16	508.2200	11.3133	30	
	X	B17	518.3900	11.2580	30	
MS-2	X	B18	528.5700	11.1907	30	
MS-2	X	B19	538.7400	11.1119	30	
MS-2	X	B20	548.9200	11.0245	30	
MS-2	X	B21	559.0900	10.9321	30	
MS-2	X	B22	569.2700	10.8368	30	
MS-2	X	B23	579.4500	10.7407	30	
MS-2	X	B24	589.6200	10.6482	30	
MS-2	X	B25	599.8000	10.5607	30	
	X	B26	609.9700	10.4823	30	
	X	B27	620.1500	10.4147	30	
MS-3	X	B28	630.3200	10.3595	30	
MS-3	X	B29	640.5000	10.3188	30	
MS-3	X	B30	650.6700	10.2942	30	
MS-3	X	B31	660.8500	10.2856	30	
MS-3	X	B32	671.0200	10.2980	30	
MS-3	X	B33	681.2000	10.3349	30	
		B34	691.3700	10.3909	30	
		B35	701.5500	10.4592	30	
		B36	711.7200	10.5322	30	
		B37	721.9000	10.6004	30	
		B38	732.0700	10.6562	30	
		B39	742.2500	10.6933	30	
		B40	752.4300	10.7058	30	

	B41	762.6000	10.7276	30	
MS-4	B42	772.7800	10.7907	30	
MS-4	B43	782.9500	10.8833	30	
MS-4	B44	793.1300	10.9938	30	
MS-4	B45	803.3000	11.1044	30	
	B46	813.4800	11.1980	30	
	B47	823.6500	11.2600	30	
	B48	833.8300	11.2824	30	
MS-4'	B49	844.0000	11.2822	30	
MS-4'	B71	851.9200	11.0457	30	X
MS-4'	B50	854.1800	11.2816	30	
MS-4'	B72	862.0100	11.0457	30	X
MS-4'	B51	864.3500	11.2809	30	
MS-4'	B73	872.1000	11.0457	30	X
MS-4'	B52	874.5300	11.2797	30	
MS-4'	B74	882.1900	11.0457	30	X
MS-4'	B53	884.7000	11.2782	30	
	B75	892.2800	11.0457	30	X
	B54	894.8800	11.2771	30	
	B76	902.3600	11.0457	30	X
	B55	905.0500	11.2765	30	
	B77	912.4500	11.0457	30	
	B56	915.2300	11.2756	30	
	B78	922.5400	11.0457	30	
	B57	925.4100	11.2754	30	
	B79	932.6400	11.0457	30	
	B58	935.5800	11.2754	30	X
	B80	942.7300	11.0457	30	
	B59	945.7600	11.2754	30	X
	B81	952.8200	11.0457	30	
	B60	955.9300	11.2754	30	X
	B82	962.9100	11.0457	30	
	B61	966.1100	11.2754	30	X
	B83	972.9900	11.0457	30	
	B62	976.2800	11.2754	30	X
	B84	983.0800	11.0457	30	
	B63	986.4600	11.2754	30	X
	B85	993.1700	11.0457	30	
	B64	996.6300	11.2754	30	X
	B86	1003.3000	11.0457	30	
	B65	1006.8100	11.2754	30	X
	B87	1013.3000	11.0457	30	
	B66	1016.9800	11.2754	30	X
	B88	1023.4000	11.0451	30	
	B67	1027.1600	11.2754	30	X
	B89	1033.4900	11.0423	30	
	B68	1037.3300	11.2754	30	X
	B90	1043.5900	11.0372	30	
	B69	1047.5100	11.2754	30	X
	B91	1053.6900	11.0302	30	
	B70	1057.6800	11.2754	30	X

	B92	1063.7900	11.0218	30
	B93	1073.8900	11.0122	30
	B94	1083.9900	11.0013	30
	B95	1094.0900	10.9871	30
	B96	1104.1900	10.9732	30
	B97	1114.1900	10.9572	30
	B98	1124.2800	10.9418	30
	B99	1134.3800	10.9248	30
	B100	1144.4800	10.9065	30
	B101	1154.5800	10.8884	30
	B102	1164.6800	10.8696	30
	B103	1174.7700	10.8513	30
	B104	1184.8700	10.8335	30
	B105	1194.9700	10.8154	30
MS-5*	B106	1205.0700	10.7979	30
MS-5*	B107	1215.1700	10.7822	30
MS-5*	B108	1225.1700	10.7663	30
MS-5*	B109	1235.2700	10.7520	30
MS-5*	B110	1245.3600	10.7385	30
MS-5*	B111	1255.4600	10.7270	30
MS-5*	B112	1265.5600	10.7174	30
MS-5*	B113	1275.6600	10.7091	30
MS-5*	B114	1285.7600	10.7022	30
MS-5*	B115	1295.8600	10.6970	30
	B116	1305.9600	10.6946	30
	B117	1316.0500	10.6937	30
	B118	1326.0500	10.6949	30
	B119	1336.1500	10.6996	30
	B120	1346.2500	10.7058	30
	B121	1356.3500	10.7163	30
	B122	1366.4500	10.7283	30
	B123	1376.5500	10.7437	30
	B124	1386.6500	10.7612	30
	B125	1396.7400	10.7807	30
	B126	1406.8400	10.8034	30
	B127	1416.9400	10.8267	30
	B128	1426.9400	10.8534	30
	B129	1437.0400	10.8818	30
	B130	1447.1400	10.9110	30
	B131	1457.2300	10.9422	30
	B132	1467.3300	10.9743	30
	B133	1477.4300	11.0074	30
	B134	1487.5300	11.0414	30
	B135	1497.6300	11.0759	30
	B136	1507.7300	11.1108	30
	B137	1517.8300	11.1461	30
	B138	1527.9200	11.1811	30
	B139	1537.9200	11.2156	30
	B140	1548.0200	11.2496	30
MS-5	B141	1558.1200	11.2826	30
MS-5	B142	1568.2200	11.3146	30
MS-5	B143	1578.3200	11.3460	30
MS-5	B144	1588.4200	11.3753	30
MS-5	B145	1598.5100	11.4037	30

MS-5		B152	1669.1000	11.5404	30	
MS-5		B153	1679.2000	11.5505	30	
MS-5		B154	1689.3000	11.5580	30	
MS-5		B155	1699.4000	11.5621	30	
MS-5		B156	1709.5000	11.5634	30	
MS-5		B157	1719.6000	11.5617	30	
MS-5		B158	1729.7000	11.5563	30	
MS-5		B159	1739.7000	11.5477	30	
MS-5		B160	1749.7900	11.5346	30	
		B161	1759.8900	11.5193	30	
		B162	1769.9900	11.5002	30	
		B163	1780.0900	11.4789	30	
		B164	1790.1900	11.4548	30	
		B165	1800.2900	11.4279	30	
		B166	1810.3800	11.3994	30	
		B167	1820.4800	11.3688	30	
		B168	1830.5800	11.3366	30	
		B169	1840.5800	11.3036	30	
		B170	1850.6800	11.2696	30	
		B171	1860.7800	11.2363	30	
		B172	1870.8700	11.2007	30	
		B173	1880.9800	11.1666	30	
		B174	1891.0700	11.1333	30	
		B175	1901.1700	11.1018	30	
		B176	1911.2700	11.0714	30	
		B177	1921.3700	11.0424	30	
		B178	1931.4700	11.0155	30	
		B179	1941.5700	10.9912	30	
		B180	1951.5700	10.9698	30	
		B181	1961.6600	10.9508	30	
		B182	1971.7600	10.9355	30	
		B183	1981.8600	10.9230	30	
		B184	1991.9600	10.9139	30	
		B185	2002.0600	10.9083	30	
		B186	2012.1500	10.9069	30	
		B187	2022.2500	10.9057	30	
		B188	2032.3500	10.9013	30	
		B189	2042.4500	10.8951	30	
		B190	2052.4500	10.8854	30	
		B191	2062.5500	10.8740	30	
		B192	2072.6500	10.8591	30	
MS-7		B193	2082.7500	10.8429	30	
MS-7		B194	2092.8400	10.8242	30	
MS-7		B195	2102.9400	10.8039	30	
MS-7		B196	2113.0400	10.7820	30	
MS-7		B197	2123.1400	10.7592	30	
MS-7		B198	2133.2400	10.7342	30	
MS-7		B199	2143.3400	10.7092	30	
MS-7		B200	2153.3400	10.6834	30	
MS-7		B201	2163.4300	10.6572	30	
MS-7		B202	2173.5300	10.6312	30	
MS-7		B203	2183.6300	10.6052	30	
MS-7		B204	2193.7300	10.5803	30	
MS-7		B205	2203.8300	10.5560	30	
MS-7		B206	2213.9300	10.5328	30	
MS-7		B207	2224.0300	10.5101	30	
MS-7		B208	2234.1200	10.4904	30	
MS-7		B209	2244.2200	10.4722	30	

MS-7		B210	2254.2200	10.4552	30	
MS-7		B211	2264.3200	10.4408	30	
MS-7		B212	2274.4200	10.4285	30	
MS-7		B213	2284.5200	10.4197	30	
MS-7		B214	2294.6100	10.4129	30	
MS-7		B215	2304.7100	10.4088	30	
MS-7		B216	2314.8100	10.4077	30	
MS-7		B217	2324.9100	10.4077	30	
MS-7		B218	2335.0100	10.4077	30	
MS-7		B219	2345.1100	10.4077	30	
		B220	2355.2100	10.4077	30	
		B221	2365.2000	10.4077	30	
		B222	2375.3000	10.4077	30	
		B223	2385.4000	10.4077	30	
		B224	2395.5000	10.4077	30	
		B225	2405.6000	10.4077	30	X
		B226	2415.7000	10.4077	30	X
		B227	2425.8000	10.4077	30	X
		B228	2435.8900	10.4077	30	X
		B229	2445.9900	10.4077	30	X
		B230	2456.0900	10.4077	30	X
		B231	2466.0900	10.4077	30	X
		B232	2476.1900	10.4077	30	X
		B233	2486.2900	10.4077	30	X
		B234	2496.3900	10.4077	30	X
		B235	2506.4800	10.4077	30	X
		B236	2516.5900	10.4077	30	X
		B237	2526.6800	10.4077	30	X
		B238	2536.7800	10.4077	30	X
		B239	2546.8800	10.4077	30	X
		B240	2556.9800	10.4077	30	X
		B241	2566.9800	10.4077	30	X
		B242	2577.0800	10.4077	30	X

Appendix C.

Earth-Sun distance in astronomical units for Julian days.

Julian Day	Distance								
1	0.9832	74	0.9945	152	1.0140	227	1.0128	305	0.9925
15	0.9836	91	0.9993	166	1.0158	242	1.0092	319	0.9892
32	0.9853	106	1.0033	182	1.0167	258	1.0057	335	0.9860
46	0.9878	121	1.0076	196	1.0165	274	1.0011	349	0.9843
60	0.9909	135	1.0109	213	1.0149	288	0.9972	365	0.9833

Appendix D.

Mean solar exoatmospheric irradiances for Hyperion channels

HYPERION Bands	Spectral Irradiances (W/m ² -μ)	HYPERION Bands	Spectral Irradiances (W/m ² -μ)
b1_355.590	949.37	b45_803.30	1128.16
b2_365.760	1158.78	b46_813.48	1108.48
b3_375.940	1061.25	b47_823.65	1068.5
b4_386.110	955.12	b48_833.83	1039.7
b5_396.290	970.87	b49_844.00	1023.84
b6_406.460	1663.73	b71_851.92	964.6
b7_416.640	1722.92	b50_854.18	938.96
b8_426.820	1650.52	b72_862.01	982.06
b9_436.990	1714.9	b51_864.35	949.97
b10_447.17	1994.52	b73_872.10	954.03
b11_457.34	2034.72	b52_874.53	949.74
b12_467.52	1970.12	b74_882.19	931.81
b13_477.69	2036.22	b53_884.70	929.54
b14_487.87	1860.24	b75_892.28	923.35
b15_498.04	1953.29	b54_894.88	917.32
b16_508.22	1953.55	b76_902.36	894.62
b17_518.39	1804.56	b55_905.05	892.69
b18_528.57	1905.51	b77_912.45	876.1
b19_538.74	1877.5	b56_915.23	877.59
b20_548.92	1883.51	b78_922.54	839.34
b21_559.09	1821.99	b57_925.41	834.6
b22_569.27	1841.92	b79_932.64	841.54
b23_579.45	1847.51	b58_935.58	837.11
b24_589.62	1779.99	b80_942.73	810.2
b25_599.80	1761.45	b59_945.76	814.7
b26_609.97	1740.8	b81_952.82	802.22
b27_620.15	1708.88	b60_955.93	788.04
b28_630.32	1672.09	b82_962.91	784.44
b29_640.50	1632.83	b61_966.11	778.2
b30_650.67	1591.92	b83_972.99	772.22
b31_660.85	1557.66	b62_976.28	764.29
b32_671.02	1525.41	b84_983.08	758.6
b33_681.20	1470.93	b63_986.46	751.28
b34_691.37	1450.37	b85_993.17	743.88
b35_701.55	1393.18	b64_996.63	740.25
b36_711.72	1372.75	b86_1003.3	721.76
b37_721.90	1235.63	b65_1006.8	710.54
b38_732.07	1266.13	b87_1013.3	714.26
b39_742.25	1279.02	b66_1016.9	703.56
b40_752.43	1265.22	b88_1023.4	698.69
b41_762.60	1235.37	b67_1027.1	695.1
b42_772.78	1202.29	b89_1033.4	682.41
b43_782.95	1194.08	b68_1037.3	676.9
b44_793.13	1143.6	b90_1043.5	669.61

HYPERION Bands	Spectral Irradiances (W/m ² -μ)	HYPERION Bands	Spectral Irradiances (W/m ² -μ)
b69_1047.5	661.9	b133_1477.	300.52
b91_1053.6	657.86	b134_1487.	292.27
b70_1057.6	649.64	b135_1497.	293.28
b92_1063.7	643.48	b136_1507.	282.14
b93_1073.8	623.13	b137_1517.	285.6
b94_1083.9	603.89	b138_1527.	280.41
b95_1094.0	582.63	b139_1537.	275.87
b96_1104.1	579.58	b140_1548.	271.97
b97_1114.1	571.8	b141_1558.	265.73
b98_1124.2	562.3	b142_1568.	260.2
b99_1134.3	551.4	b143_1578.	251.62
b100_1144.	540.52	b144_1588.	244.11
b101_1154.	534.17	b145_1598.	247.83
b102_1164.	519.74	b146_1608.	242.85
b103_1174.	511.29	b147_1618.	238.15
b104_1184.	497.28	b148_1628.	239.29
b105_1194.	492.82	b149_1638.	227.38
b106_1205.	479.41	b150_1648.	226.69
b107_1215.	479.56	b151_1659.	225.48
b108_1225.	469.01	b152_1669.	218.69
b109_1235.	461.6	b153_1679.	209.07
b110_1245.	451	b154_1689.	210.62
b111_1255.	444.06	b155_1699.	206.98
b112_1265.	435.25	b156_1709.	201.59
b113_1275.	429.29	b157_1719.	198.09
b114_1285.	415.69	b158_1729.	191.77
b115_1295.	412.87	b159_1739.	184.02
b116_1305.	405.4	b160_1749.	184.91
b117_1316.	396.94	b161_1759.	182.75
b118_1326.	391.94	b162_1769.	180.09
b119_1336.	386.79	b163_1780.	175.18
b120_1346.	380.65	b164_1790.	173
b121_1356.	370.96	b165_1800.	168.87
b122_1366.	365.57	b166_1810.	165.19
b123_1376.	358.42	b167_1820.	156.3
b124_1386.	355.18	b168_1830.	159.01
b125_1396.	349.04	b169_1840.	155.22
b126_1406.	342.1	b170_1850.	152.62
b127_1416.	336	b171_1860.	149.14
b128_1426.	325.94	b172_1870.	141.63
b129_1437.	325.71	b173_1880.	139.43
b130_1447.	318.27	b174_1891.	139.22
b131_1457.	312.12	b175_1901.	137.97
b132_1467.	308.08	b176_1911.	136.73

HYPERION Bands	Spectral Irradiances (W/m ² -μ)	HYPERION Bands	Spectral Irradiances (W/m ² -μ)
b177_1921.	133.96	b216_2314.	68.28
b178_1931.	130.29	b217_2324.	66.39
b179_1941.	124.5	b218_2335.	65.76
b180_1951.	124.75	b219_2345.	65.23
b181_1961.	123.92	b220_2355.	63.09
b182_1971.	121.95	b221_2365.	62.9
b183_1981.	118.96	b222_2375.	61.68
b184_1991.	117.78	b223_2385.	60
b185_2002.	115.56	b224_2395.	59.94
b186_2012.	114.52	b225_2405.	59.18
b187_2022.	111.65	b226_2415.	57.38
b188_2032.	109.21	b227_2425.	57.1
b189_2042.	107.69	b228_2435.	56.25
b190_2052.	106.13	b229_2445.	55.09
b191_2062.	103.7	b230_2456.	54.02
b192_2072.	102.42	b231_2466.	53.75
b193_2082.	100.42	b232_2476.	52.78
b194_2092.	98.27	b233_2486.	51.6
b195_2102.	97.37	b234_2496.	51.44
b196_2113.	95.44	b235_2506.	0
b197_2123.	93.55	b236_2516.	0
b198_2133.	92.35	b237_2526.	0
b199_2143.	90.93	b238_2536.	0
b200_2153.	89.37	b239_2546.	0
b201_2163.	84.64	b240_2556.	0
b202_2173.	85.47	b241_2566.	0
b203_2183.	84.49	b242_2577.	0
b204_2193.	83.43		
b205_2203.	81.62		
b206_2213.	80.67		
b207_2224.	79.32		
b208_2234.	78.11		
b209_2244.	76.69		
b210_2254.	75.35		
b211_2264.	74.15		
b212_2274.	73.25		
b213_2284.	71.67		
b214_2294.	70.13		
b215_2304.	69.52		

Appendix E.

Hyperion metadata file (2007.07.19, New Mexico)

```
GROUP = L1_METADATA_FILE
GROUP = METADATA_FILE_INFO
REQUEST_ID = "0330372007200_20001"
PRODUCT_CREATION_TIME = 2009-06-19T16:55:06Z
EO1_XBAND = "1"
GROUND_STATION = "SGS"
DPS_VERSION_NUMBER = "3.00"
DATEHOUR_CONTACT_PERIOD = 0720018
END_GROUP = METADATA_FILE_INFO
GROUP = PRODUCT_METADATA
PRODUCT_TYPE = "L1GST"
PROCESSING_SOFTWARE = "EPG_3.1.2"
EPHEMERIS_TYPE = "DEFINITIVE"
SPACECRAFT_ID = "EO1"
SENSOR_ID = "HYPERION"
ACQUISITION_DATE = 2007-07-19
START_TIME = 2007 200 17:16:34
END_TIME = 2007 200 17:21:12
PRODUCT_UL_CORNER_LAT = 33.701827
PRODUCT_UL_CORNER_LON = -106.406356
PRODUCT_UR_CORNER_LAT = 33.686578
PRODUCT_UR_CORNER_LON = -106.318263
PRODUCT_LL_CORNER_LAT = 31.831443
PRODUCT_LL_CORNER_LON = -106.863612
PRODUCT_LR_CORNER_LAT = 31.816353
PRODUCT_LR_CORNER_LON = -106.777336
PRODUCT_UL_CORNER_MAPX = 324900.000000
PRODUCT_UL_CORNER_MAPY = 3740100.000000
PRODUCT_UR_CORNER_MAPX = 381000.000000
PRODUCT_UR_CORNER_MAPY = 3740100.000000
PRODUCT_LL_CORNER_MAPX = 324900.000000
PRODUCT_LL_CORNER_MAPY = 3528000.000000
PRODUCT_LR_CORNER_MAPX = 381000.000000
PRODUCT_LR_CORNER_MAPY = 3528000.000000
PRODUCT_SAMPLES = 1871
PRODUCT_LINES = 7071
BAND1_FILE_NAME = "EO1H0330372007200110K7_B001_L1T.TIF"
BAND2_FILE_NAME = "EO1H0330372007200110K7_B002_L1T.TIF"
BAND3_FILE_NAME = "EO1H0330372007200110K7_B003_L1T.TIF"
BAND4_FILE_NAME = "EO1H0330372007200110K7_B004_L1T.TIF"
BAND5_FILE_NAME = "EO1H0330372007200110K7_B005_L1T.TIF"
BAND6_FILE_NAME = "EO1H0330372007200110K7_B006_L1T.TIF"
BAND7_FILE_NAME = "EO1H0330372007200110K7_B007_L1T.TIF"
BAND8_FILE_NAME = "EO1H0330372007200110K7_B008_L1T.TIF"
BAND9_FILE_NAME = "EO1H0330372007200110K7_B009_L1T.TIF"
BAND10_FILE_NAME = "EO1H0330372007200110K7_B010_L1T.TIF"
BAND11_FILE_NAME = "EO1H0330372007200110K7_B011_L1T.TIF"
BAND12_FILE_NAME = "EO1H0330372007200110K7_B012_L1T.TIF"
BAND13_FILE_NAME = "EO1H0330372007200110K7_B013_L1T.TIF"
BAND14_FILE_NAME = "EO1H0330372007200110K7_B014_L1T.TIF"
BAND15_FILE_NAME = "EO1H0330372007200110K7_B015_L1T.TIF"
BAND16_FILE_NAME = "EO1H0330372007200110K7_B016_L1T.TIF"
BAND17_FILE_NAME = "EO1H0330372007200110K7_B017_L1T.TIF"
BAND18_FILE_NAME = "EO1H0330372007200110K7_B018_L1T.TIF"
BAND19_FILE_NAME = "EO1H0330372007200110K7_B019_L1T.TIF"
BAND20_FILE_NAME = "EO1H0330372007200110K7_B020_L1T.TIF"
BAND21_FILE_NAME = "EO1H0330372007200110K7_B021_L1T.TIF"
BAND22_FILE_NAME = "EO1H0330372007200110K7_B022_L1T.TIF"
BAND23_FILE_NAME = "EO1H0330372007200110K7_B023_L1T.TIF"
BAND24_FILE_NAME = "EO1H0330372007200110K7_B024_L1T.TIF"
BAND25_FILE_NAME = "EO1H0330372007200110K7_B025_L1T.TIF"
BAND26_FILE_NAME = "EO1H0330372007200110K7_B026_L1T.TIF"
BAND27_FILE_NAME = "EO1H0330372007200110K7_B027_L1T.TIF"
BAND28_FILE_NAME = "EO1H0330372007200110K7_B028_L1T.TIF"
BAND29_FILE_NAME = "EO1H0330372007200110K7_B029_L1T.TIF"
BAND30_FILE_NAME = "EO1H0330372007200110K7_B030_L1T.TIF"
BAND31_FILE_NAME = "EO1H0330372007200110K7_B031_L1T.TIF"
```


BAND180_FILE_NAME = "EO1H0330372007200110K7_B180_L1T.TIF"
BAND181_FILE_NAME = "EO1H0330372007200110K7_B181_L1T.TIF"
BAND182_FILE_NAME = "EO1H0330372007200110K7_B182_L1T.TIF"
BAND183_FILE_NAME = "EO1H0330372007200110K7_B183_L1T.TIF"
BAND184_FILE_NAME = "EO1H0330372007200110K7_B184_L1T.TIF"
BAND185_FILE_NAME = "EO1H0330372007200110K7_B185_L1T.TIF"
BAND186_FILE_NAME = "EO1H0330372007200110K7_B186_L1T.TIF"
BAND187_FILE_NAME = "EO1H0330372007200110K7_B187_L1T.TIF"
BAND188_FILE_NAME = "EO1H0330372007200110K7_B188_L1T.TIF"
BAND189_FILE_NAME = "EO1H0330372007200110K7_B189_L1T.TIF"
BAND190_FILE_NAME = "EO1H0330372007200110K7_B190_L1T.TIF"
BAND191_FILE_NAME = "EO1H0330372007200110K7_B191_L1T.TIF"
BAND192_FILE_NAME = "EO1H0330372007200110K7_B192_L1T.TIF"
BAND193_FILE_NAME = "EO1H0330372007200110K7_B193_L1T.TIF"
BAND194_FILE_NAME = "EO1H0330372007200110K7_B194_L1T.TIF"
BAND195_FILE_NAME = "EO1H0330372007200110K7_B195_L1T.TIF"
BAND196_FILE_NAME = "EO1H0330372007200110K7_B196_L1T.TIF"
BAND197_FILE_NAME = "EO1H0330372007200110K7_B197_L1T.TIF"
BAND198_FILE_NAME = "EO1H0330372007200110K7_B198_L1T.TIF"
BAND199_FILE_NAME = "EO1H0330372007200110K7_B199_L1T.TIF"
BAND200_FILE_NAME = "EO1H0330372007200110K7_B200_L1T.TIF"
BAND201_FILE_NAME = "EO1H0330372007200110K7_B201_L1T.TIF"
BAND202_FILE_NAME = "EO1H0330372007200110K7_B202_L1T.TIF"
BAND203_FILE_NAME = "EO1H0330372007200110K7_B203_L1T.TIF"
BAND204_FILE_NAME = "EO1H0330372007200110K7_B204_L1T.TIF"
BAND205_FILE_NAME = "EO1H0330372007200110K7_B205_L1T.TIF"
BAND206_FILE_NAME = "EO1H0330372007200110K7_B206_L1T.TIF"
BAND207_FILE_NAME = "EO1H0330372007200110K7_B207_L1T.TIF"
BAND208_FILE_NAME = "EO1H0330372007200110K7_B208_L1T.TIF"
BAND209_FILE_NAME = "EO1H0330372007200110K7_B209_L1T.TIF"
BAND210_FILE_NAME = "EO1H0330372007200110K7_B210_L1T.TIF"
BAND211_FILE_NAME = "EO1H0330372007200110K7_B211_L1T.TIF"
BAND212_FILE_NAME = "EO1H0330372007200110K7_B212_L1T.TIF"
BAND213_FILE_NAME = "EO1H0330372007200110K7_B213_L1T.TIF"
BAND214_FILE_NAME = "EO1H0330372007200110K7_B214_L1T.TIF"
BAND215_FILE_NAME = "EO1H0330372007200110K7_B215_L1T.TIF"
BAND216_FILE_NAME = "EO1H0330372007200110K7_B216_L1T.TIF"
BAND217_FILE_NAME = "EO1H0330372007200110K7_B217_L1T.TIF"
BAND218_FILE_NAME = "EO1H0330372007200110K7_B218_L1T.TIF"
BAND219_FILE_NAME = "EO1H0330372007200110K7_B219_L1T.TIF"
BAND220_FILE_NAME = "EO1H0330372007200110K7_B220_L1T.TIF"
BAND221_FILE_NAME = "EO1H0330372007200110K7_B221_L1T.TIF"
BAND222_FILE_NAME = "EO1H0330372007200110K7_B222_L1T.TIF"
BAND223_FILE_NAME = "EO1H0330372007200110K7_B223_L1T.TIF"
BAND224_FILE_NAME = "EO1H0330372007200110K7_B224_L1T.TIF"
BAND225_FILE_NAME = "EO1H0330372007200110K7_B225_L1T.TIF"
BAND226_FILE_NAME = "EO1H0330372007200110K7_B226_L1T.TIF"
BAND227_FILE_NAME = "EO1H0330372007200110K7_B227_L1T.TIF"
BAND228_FILE_NAME = "EO1H0330372007200110K7_B228_L1T.TIF"
BAND229_FILE_NAME = "EO1H0330372007200110K7_B229_L1T.TIF"
BAND230_FILE_NAME = "EO1H0330372007200110K7_B230_L1T.TIF"
BAND231_FILE_NAME = "EO1H0330372007200110K7_B231_L1T.TIF"
BAND232_FILE_NAME = "EO1H0330372007200110K7_B232_L1T.TIF"
BAND233_FILE_NAME = "EO1H0330372007200110K7_B233_L1T.TIF"
BAND234_FILE_NAME = "EO1H0330372007200110K7_B234_L1T.TIF"
BAND235_FILE_NAME = "EO1H0330372007200110K7_B235_L1T.TIF"
BAND236_FILE_NAME = "EO1H0330372007200110K7_B236_L1T.TIF"
BAND237_FILE_NAME = "EO1H0330372007200110K7_B237_L1T.TIF"
BAND238_FILE_NAME = "EO1H0330372007200110K7_B238_L1T.TIF"
BAND239_FILE_NAME = "EO1H0330372007200110K7_B239_L1T.TIF"
BAND240_FILE_NAME = "EO1H0330372007200110K7_B240_L1T.TIF"
BAND241_FILE_NAME = "EO1H0330372007200110K7_B241_L1T.TIF"
BAND242_FILE_NAME = "EO1H0330372007200110K7_B242_L1T.TIF"
METADATA_L1_FILE_NAME = "EO1H0330372007200110K7_MTL.L1T"
CPF_FILE_NAME = "EO1ACPF20070502_20070815.01"
END_GROUP = PRODUCT_METADATA
GROUP = RADIANCE_SCALING
SCALING_FACTOR_VNIR = 40
SCALING_FACTOR_SWIR = 80
END_GROUP = RADIANCE_SCALING
GROUP = PRODUCT_PARAMETERS
CORRECTION_METHOD_GAIN = "NONE"
CORRECTION_METHOD_BIAS = "NONE"
SENSOR_LOOK_ANGLE = -16.277

```
SUN_AZIMUTH = 108.097715
SUN_ELEVATION = 62.0355
OUTPUT_FORMAT = "GEOTIFF"
END_GROUP = PRODUCT_PARAMETERS
GROUP = CORRECTIONS_APPLIED
  ABNORMAL_PIXELS = "Y"
  INOPERABLE_DETECTORS = "Y"
  STRIPING = "N"
  ELEVATION_SOURCE = "SRTM-2"
END_GROUP = CORRECTIONS_APPLIED
GROUP = PROJECTION_PARAMETERS
  REFERENCE_DATUM = "WGS84"
  REFERENCE_ELLIPSOID = "WGS84"
  GRID_CELL_SIZE = 30.00
  ORIENTATION = "NUP"
  RESAMPLING_OPTION = "CC"
  MAP_PROJECTION = "UTM"
END_GROUP = PROJECTION_PARAMETERS
GROUP = UTM_PARAMETERS
  ZONE_NUMBER = 13
END_GROUP = UTM_PARAMETERS
END_GROUP = L1_METADATA_FILE
END
```

Appendix F

Real AVHRR NDVI biweekly composites, 1 km resolution data (Earth Explorer product)¹⁸

No.	ID	Date
1	us07_002008	2007.01.01 – 2007.01.08*
2	us07_009022	2007.01.09 – 2007.01.21
3	us07_023036	2007.01.23 – 2007.02.05
4	us07_037050	2007.02.06 – 2007.02.19
5	us07_051064	2007.02.20 – 2007.03.05
6	us07_065078	2007.03.07 – 2007.03.19
7	us07_079092	2007.03.20 – 2007.04.02
8	us07_093106	2007.04.03 - 2007.04.16
9	us07_107120	2007.04.17 - 2007.04.30
10	us07_121134	2007.05.01 - 2007.05.14
11	us07_135148	2007.05.15 - 2007.05.28
12	us07_149162	2007.05.29 - 2007.06.11
13	us07_163176	2007.06.12 - 2007.06.24
14	us07_177190	2007.06.26 - 2007.07.08
15	us07_191204	2007.07.10 - 2007.07.23
16	us07_205218	2007.07.24 - 2007.08.06
17	us07_219232	2007.08.07 - 2007.08.20
18	us07_233246	2007.08.21 - 2007.09.03
19	us07_247260	2007.09.04 - 2007.09.17
20	us07_261274	2007.09.18 - 2007.10.01
21	us07_275288	2007.10.02 - 2007.10.14
22	us07_289302	2007.10.16 - 2007.10.29
23	us07_303316	2007.10.30 - 2007.11.12
24	us07_317330	2007.11.13 - 2007.11.26
25	us07_331344	2007.11.27 - 2007.12.10
26	us07_345358	2007.12.11 - 2007.12.23

* The first AVHRR NDVI data is weekly instead of biweekly.

¹⁸ Source: <http://edcsns17.cr.usgs.gov/EarthExplorer/>

Real MODIS NDVI 16-day composites, 250 m resolution (MYD13Q1 Product)¹⁹

No.	Date	No.	Date
1	2007.01.09	13	2007.07.20
2	2007.01.25	14	2007.08.05
3	2007.02.10	15	2007.08.21
4	2007.02.26	16	2007.09.06
5	2007.03.14	17	2007.09.22
6	2007.03.30	18	2007.10.08
7	2007.04.15	19	2007.10.24
8	2007.05.01	20	2007.11.09
9	2007.05.17	21	2007.11.25
10	2007.06.02	22	2007.12.11
11	2007.06.18	23	2007.12.27
12	2007.07.04		

Real MODIS NDVI 16-day composites, 250 m resolution (MOD13Q1 Product)²⁰

No.	Date	No.	Date
1	2007.01.01	13	2007.07.12
2	2007.01.17	14	2007.07.28
3	2007.02.02	15	2007.08.13
4	2007.02.18	16	2007.08.29
5	2007.03.06	17	2007.09.14
6	2007.03.22	18	2007.09.30
7	2007.04.07	19	2007.10.16
8	2007.04.23	20	2007.11.01
9	2007.05.09	21	2007.11.17
10	2007.05.25	22	2007.12.03
11	2007.06.10	23	2007.12.19
12	2007.06.26		

¹⁹ Source:

https://lpdaac.usgs.gov/lpdaac/products/modis_products_table/vegetation_indices/16_day_l3_global_250m/myd13q1

²⁰ Source:

http://daac.ornl.gov/glb_viz_2/28Sep2010_16:40:48_141959772L32.18504L-106.743S1L1_MOD13Q1/index.html

Institutionen av naturgeografi och ekosystemvetenskap, Lunds Universitet.

Student examensarbete (Seminarieuppsatser). Uppsatserna finns tillgängliga på institutionens geobibliotek, Sölvegatan 12, 223 62 LUND. Serien startade 1985. Hela listan och själva uppsatserna är även tillgängliga på LUP student papers (www.nateko.lu.se/masterthesis) och via Geobiblioteket (www.geobib.lu.se)

The student thesis reports are available at the Geo-Library, Department of Physical Geography, University of Lund, Sölvegatan 12, S-223 62 Lund, Sweden. Report series started 1985. The complete list and electronic versions are also electronic available at the LUP student papers (www.nateko.lu.se/masterthesis) and through the Geo-library (www.geobib.lu.se)

- 175 Hongxiao Jin (2010): Drivers of Global Wildfires — Statistical analyses
- 176 Emma Cederlund (2010): Dalby Söderskog – Den historiska utvecklingen
- 177 Lina Glad (2010): En förändringsstudie av Ivösjöns strandlinje
- 178 Erika Filppa (2010): Utsläpp till luft från ballastproduktionen år 2008
- 179 Karolina Jacobsson (2010): Havsisens avsmältning i Arktis och dess effekter
- 180 Mattias Spångmyr (2010): Global of effects of albedo change due to urbanization
- 181 Emmelie Johansson & Towe Andersson (2010): Ekologiskt jordbruk - ett sätt att minska övergödningen och bevara den biologiska mångfalden?
- 182 Åsa Cornander (2010): Stigande havsnivåer och dess effect på känsligt belägna bosättningar
- 183 Linda Adamsson (2010): Landskapsekologisk undersökning av ädellövskogen i Östra Vätterbranterna
- 184 Ylva Persson (2010): Markfuktighetens påverkan på granens tillväxt i Guvarp
- 185 Boel Hedgren (2010): Den arktiska permafrostens degradering och metangasutsläpp
- 186 Joakim Lindblad & Johan Lindenbaum (2010): GIS-baserad kartläggning av sambandet mellan pesticidförekomster i grundvatten och markegenskaper
- 187 Oscar Dagerskog (2010): Baösbergsgrottan – Historiska tillbakablickar och en lokalklimatologisk undersökning
- 188 Mikael Månsson (2010): Webbaserad GIS-klient för hantering av geologisk information
- 189 Lina Eklund (2010): Accessibility to health services in the West Bank, occupied Palestinian Territory.
- 190 Edvin Eriksson (2010): Kvalitet och osäkerhet i geografisk analys - En studie om kvalitetsaspekter med fokus på osäkerhetsanalys av rumslig prognosmodell för trafikolyckor
- 191 Elsa Tessaire (2010): Impacts of stressful weather events on forest ecosystems in south Sweden.
- 192 Xuejing Lei (2010): Assessment of Climate Change Impacts on Cork Oak in Western Mediterranean Regions: A Comparative Analysis of Extreme Indices
- 193 Radoslaw Guzinski (2010): Comparison of vegetation indices to determine their accuracy in predicting spring phenology of Swedish ecosystems
- 194 Yasar Arfat (2010): Land Use / Land Cover Change Detection and Quantification — A Case study in Eastern Sudan
- 195 Ling Bai (2010): Comparison and Validation of Five Global Land Cover Products Over African Continent

- 196 Raunaq Jahan (2010): Vegetation indices, FAPAR and spatial seasonality
analysis of crops in southern Sweden
- 197 Masoumeh Ghadiri (2010): Potential of Hyperion imagery for simulation of
MODIS NDVI and AVHRR-consistent NDVI time series in a semi-arid region
- 198 Maoela A. Malebajoa (2010): Climate change impacts on crop yields and
adaptive measures for agricultural sector in the lowlands of Lesotho
- 199 Herbert Mbufong Njuabe (2011): Subarctic Peatlands in a Changing Climate:
Greenhouse gas response to experimentally increased snow cover
- 200 Naemi Gunlycke & Anja Tuomaala (2011): Detecting forest degradation in
Marakwet district, Kenya, using remote sensing and GIS
- 201 Nzung Seraphine Ebang (2011): How was the carbon balance of Europe
affected by the summer 2003 heat wave? A study based on the use of a
Dynamic Global Vegetation Model; LPJ-GUESS
- 202 Per-Ola Olsson (2011): Cartography in Internet-based view services – methods
to improve cartography when geographic data from several sources are
combined
- 203 Kristoffer Mattisson (2011): Modelling noise exposure from roads – a case
study in Burlövs municipality
- 204 Erik Ahlberg (2011): BVOC emissions from a subarctic Mountain birch:
Analysis of short-term chamber measurements.
- 205 Wilbert Timiza (2011): Climate variability and satellite – observed vegetation
responses in Tanzania.
- 206 Louise Svensson (2011): The ethanol industry - impact on land use and
biodiversity. A case study of São Paulo State in Brazil.
- 207 Fredrik Fredén (2011): Impacts of dams on lowland agriculture in the Mekong
river catchment.
- 208 Johanna Hjärpe (2011): Kartläggning av kväve i vatten i LKAB:s verksamhet i
Malmberget år 2011 och kvävetets betydelse i akvatiska ekosystem ur ett lokalt
och ett globalt perspektiv
- 209 Oskar Löfgren (2011): Increase of tree abundance between 1960 and 2009 in
the treeline of Luongastunturi in the northern Swedish Scandes
- 210 Izabella Rosengren (2011): Land degradation in the Ovitoto region of
Namibia: what are the local causes and consequences and how do we avoid
them?
- 211 Irina Popova (2011): Agroforestry och dess påverkan på den biofysiska miljön
i Afrika.
- 212 Emilie Walsund (2011): Food Security and Food Sufficiency in Ethiopia and
Eastern Africa.
- 213 Martin Bernhardson (2011): Jökulhlaups: Their Associated Landforms and
Landscape Impacts.
- 214 Michel Tholin (2011): Weather induced variations in raptor migration; A study
of raptor migration during one autumn season in Kazbegi, Georgia, 2010
- 215 Amelie Lindgren (2011) The Effect of Natural Disturbances on the Carbon
Balance of Boreal Forests.
- 216 Klara Århem (2011): Environmental consequences of the palm oil industry in
Malaysia.
- 217 Ana Maria Yáñez Serrano (2011) Within-Canopy Sesquiterpene Ozonolysis in
Amazonia
- 218 Edward Kashava Kuliwoye (2011) Flood Hazard Assessment by means of
Remote Sensing and Spatial analyses in the Cuvelai Basin Case Study

- Ohangwena Region –Northern Namibia
- 219 Julia Olsson (2011) GIS-baserad metod för etablering av centraliserade biogasanläggningar baserad på husdjursgödsel.
- 220 Florian Sallaba (2011) The potential of support vector machine classification of land use and land cover using seasonality from MODIS satellite data
- 221 Salem Beyene Ghezahai (2011) Assessing vegetation changes for parts of the Sudan and Chad during 2000-2010 using time series analysis of MODIS-NDVI
- 222 Bahzad Khaled (2011) Spatial heterogeneity of soil CO₂ efflux at ADVEX site Norunda in Sweden
- 223 Emmy Axelsson (2011) Spatiotemporal variation of carbon stocks and fluxes at a clear-cut area in central Sweden
- 224 Eduard Mikayelyan (2011) Developing Android Mobile Map Application with Standard Navigation Tools for Pedestrians
- 225 Johanna Engström (2011) The effect of Northern Hemisphere teleconnections on the hydropower production in southern Sweden
- 226 Kosemani Bosede Adenike (2011) Deforestation and carbon stocks in Africa
- 227 Ouattara Adama (2011) Mauritania and Senegal coastal area urbanization, ground water flood risk in Nouakchott and land use/land cover change in Mbour area
- 228 Andrea Johansson (2011) Fire in Boreal forests
- 229 Arna Björk Þorsteinsdóttir (2011) Mapping *Lupinus nootkatensis* in Iceland using SPOT 5 images
- 230 Cléber Domingos Arruda (2011) Developing a Pedestrian Route Network Service (PRNS)
- 231 Nitin Chaudhary (2011) Evaluation of RCA & RCA GUESS and estimation of vegetation-climate feedbacks over India for present climate
- 232 Bjarne Munk Lyshede (2012) Diurnal variations in methane flux in a low-arctic fen in Southwest Greenland